Direct displacement-based seismic design of glulam frames with buckling restrained braces

Wenchen Dong[a,b*], Minghao Li[a], Timothy Sullivan[a], Gregory MacRae[a], Chin-Long Lee[a], and Theodore Chang[a,c]

[a]Department of Civil and Natural Resources Engineering, University of Canterbury, New Zealand

[b]Department of Civil, Environmental and Geomatic Engineering, University College London, United Kingdom

[c]Integrative Research Institute for the Sciences (IRIS), Humboldt Univerity of Berlin, Berlin, Germany

*Corresponding Author. Email: wenchen.dong@ucl.ac.uk

Direct displacement-based seismic design of glulam frames with buckling restrained braces

Abstract

This paper presents a direct displacement-based design (DDBD) approach for the buckling restrained braces (BRBs) braced glue-laminated timber (glulam) frame (BRBGF) structures. First, the critical design parameters of the DDBD approach were derived for BRBGFs. Then, using experimentally verified numerical models, pushover analyses and nonlinear time-history analyses (NLTHA) were conducted on a series of one-storey BRBGFs to calibrate the stiffness adjustment factor λ for BRB-timber connections and the spectral displacement reduction factor η. Finally, the DDBD was verified as a prospective approach for the seismic design of multi-storey BRBGF buildings by NLTHA of the case study buildings.

Keywords: glulam frames; buckling restrained braces (BRBs); direct displacement-based design (DDBD); BRB-timber connections; nonlinear time-history analyses (NLTHA).

1 Introduction

Multi-storey mass timber buildings have gained immense popularity worldwide due to the development of engineered wood products with enhanced structural performance compared to sawn timber. These timber buildings also hold potential for generalizing climate-change mitigation and preservation [1]. However, timber has a relatively low elastic modulus compared to other construction materials such as steel and reinforced concrete. In addition, timber members are prone to brittle failure under tension with a limited energy dissipation capacity. Larger member sizes are often needed to satisfy stiffness requirements, and limited ductility is usually assumed for multi-storey mass timber buildings [2]. In earthquake-prone countries such as New Zealand, seismic considerations usually govern the design of lateral force resisting systems (LFRS) of multi-storey buildings. The limited ductility assumption may result in uneconomical member sizes and increase the amount of LFRS (e.g. shear walls and braces). Excess shear walls or braces may restrict the flexibility of architectural plans and reduce space efficiency.

Several new solutions have been proposed to overcome these limitations. One is to introduce hybrid systems that can take advantage of the strengths of different construction materials and provide suitable solutions for LFRS [3–7]. Quintana Gallo et al. [8] conducted a comprehensive review of timber-based hybrid LFRS, such as steel frames with infilled cross-laminated timber (CLT) shear walls [3], steel frames with light-timber frame shear walls [9], post-tensioned CLT shear walls with energy dissipators [6,10] and timber frames with energy dissipators [11,12]. However, timber shear walls might be more suitable for residential buildings with demands on open spaces. In addition, the post-tension loss of mass timber buildings during long-term service still requires more investigation [13]. Timber frames with energy dissipators, providing larger open spaces and relatively accessible replacement for dissipators, are still more favored for many projects. Recently, a new timber-steel hybrid system that integrates buckling restrained braces (BRBs) into glued laminated timber (glulam) frames was proposed and experimentally investigated [14]. As shown in Figure 1, dowelled connections with inserted steel plates were used to connect the glulam frame with the gusset plates, and BRBs were connected to the gusset plates by pinned connections. The BRB-braced glulam frames (BRBGFs) significantly increased energy dissipation capacity compared with conventional timber-braced glulam frames. In addition, the damage in the connections and glulam members was minimised as the capacity design approach was followed. As shown in Figure 2, initial slips were observed on the load-drift curves of the BRBGFs because the specimens used pin-end BRBs [15] and dowelled connections that required manufacturing tolerances to be installed. The experimental test data were then used to calibrate component-based numerical models in OpenSees and the modelling details are explained in [16]. The influence of connection stiffness and initial slips on the cyclic performance of the system was investigated through parametric studies. It was shown that the connections had a negligible moment-resisting capacity, and the connections designed with a connection relative overstrength factor γ = 1.5 were suitable for engaging the BRBs and protecting the glulam members and connections. In addition, the initial slips caused by the manufacturing tolerances had a negligible impact on the ultimate strength and overall energy dissipation of the BRBGFs under cyclic loading. Further information regarding previous experimental and numerical studies can be found in [14,16].

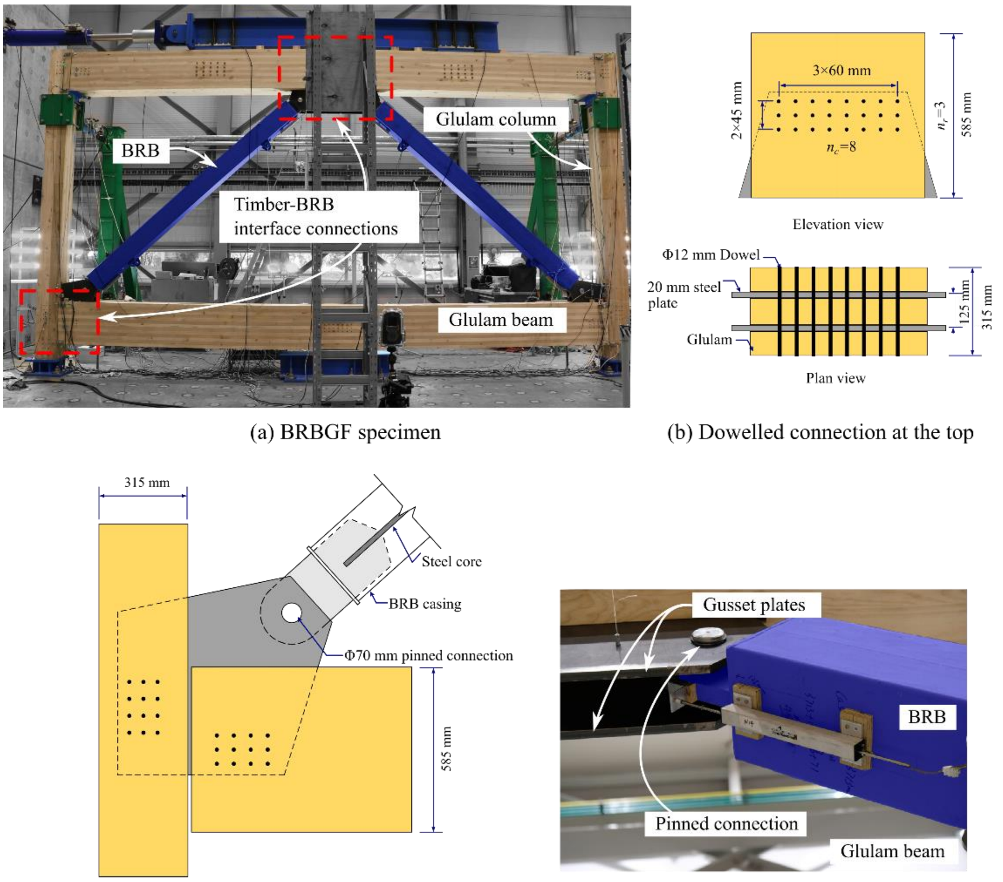

(a) BRBGF specimen (b) Dowelled connection at the top

(c) Dowelled connection at the bottom (d) Pinned connection details

Figure 1 BRBGF specimen with the dowelled connections [14]

Figure 2 shows that the numerical models of the BRBGFs can accurately predict the cyclic performance. However, the complicated modelling process and lack of necessary design parameters of this hybrid system may still restrict its practical application. In addition, the influence of initial slips under seismic ground motions requires further investigation. This study fills the research gaps for applying a direct displacement-based design (DDBD) approach [17] to the seismic design of the BRBGF structures. It provides suitable displacement profiles, stiffness adjustment for timber-steel interface connections and hysteretic modelling for DDBD. In addition, it verifies the suitability of the approach via nonlinear time-history analysis (NLTHA) of case study buildings, and thus facilitates the application of this hybrid system.

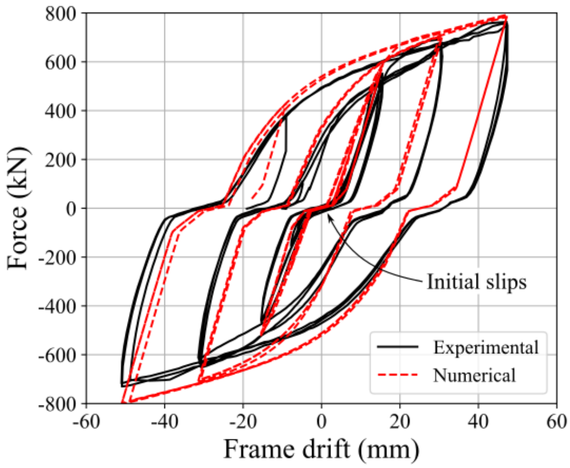

Figure 2 Comparison of BRBGF hysteresis curves [16]

2 Fundamentals of the DDBD approach

The DDBD approach was first proposed by Priestley et al. [18–20] to provide an alternative design solution for the traditional force-based design (FBD) approach widely used by modern design standards (e.g. Eurocode 8 [21] and NZS 1170.5 [22]). Previous research [17,23,24] has shown that the FBD approach may have limitations for seismic design. One limitation is that the displacement response, usually directly correlated with building damage levels [25–27] is given only secondary importance. Alternative methods have been developed to address some of the limitations of traditional FBD approaches. For example, in the New Zealand standard NZS 1170.5 [22] the designer is prompted to satisfy structural and non-structural deformation limits and check that the design ductility is compatible with the expected ductility demands. However, these standards do not require engineers to address all the issues raised by Priestley et al. [17]. For example, elastic analysis is used to calculate the inelastic force distributions in the FBD approach and the unique force reduction factor for a given structure type may be invalid [17]. Previous research has shown that the DDBD approach might benefit some conditions more than the FBD approach for nonlinear seismic design [28,29]. Consequently, the DDBD approach has been used in a variety of structural systems, including reinforced concrete structures [30–34], steel structures [24,35–39] and timber structures [40–46]. A model code for the DDBD approach was also developed for practical design guidelines [47]. For BRBGF structures, the initial slips, as shown in Figure 2, may cause difficulty in estimating the initial stiffness and fundamental period essential for the FBD approach. Therefore, the FBD approach may not be well suited to particular cases of BRBGFs. The DDBD approach implicitly assumes that a low initial stiffness will not affect the displacement demands in high intensity earthquakes by utilising the secant stiffness concept (a hypothesis that will be verified in this work). In this regard, the DDBD approach was developed for the BRBGF structures.

The primary process of the DDBD approach [17] is illustrated in Figure 3. The first step is to substitute a multi-degree-of-freedom (MDOF) structure with an equivalent single-degree-of-freedom (SDOF) system (Figure 3a). A displacement profile of the MDOF structure under seismic loads is assumed based on the knowledge of the design displacement profile. Therefore, the equivalent SDOF system characterised by its design displacement Δ_d, effective mass M_e, and effective height H_e can be calculated by Eq. 1-Eq. 3.

$$\Delta_d = \frac{\sum_{i=1}^{n} m_i \Delta_i^2}{\sum_{i=1}^{n} m_i \Delta_i} \qquad \text{Eq. 1}$$

$$M_e = \frac{\sum_{i=1}^{n} m_i \Delta_i}{\Delta_d} \qquad \text{Eq. 2}$$

$$H_e = \frac{\sum_{i=1}^{n} m_i \Delta_i H_i}{\sum_{i=1}^{n} m_i \Delta_i} \qquad \text{Eq. 3}$$

where Δ_i is the storey drift at the i-th storey (mm); m_i is the seismic mass at the i-th storey (tons); H_i is the height of the i-th storey from the ground (m); and n is the total number of storeys.

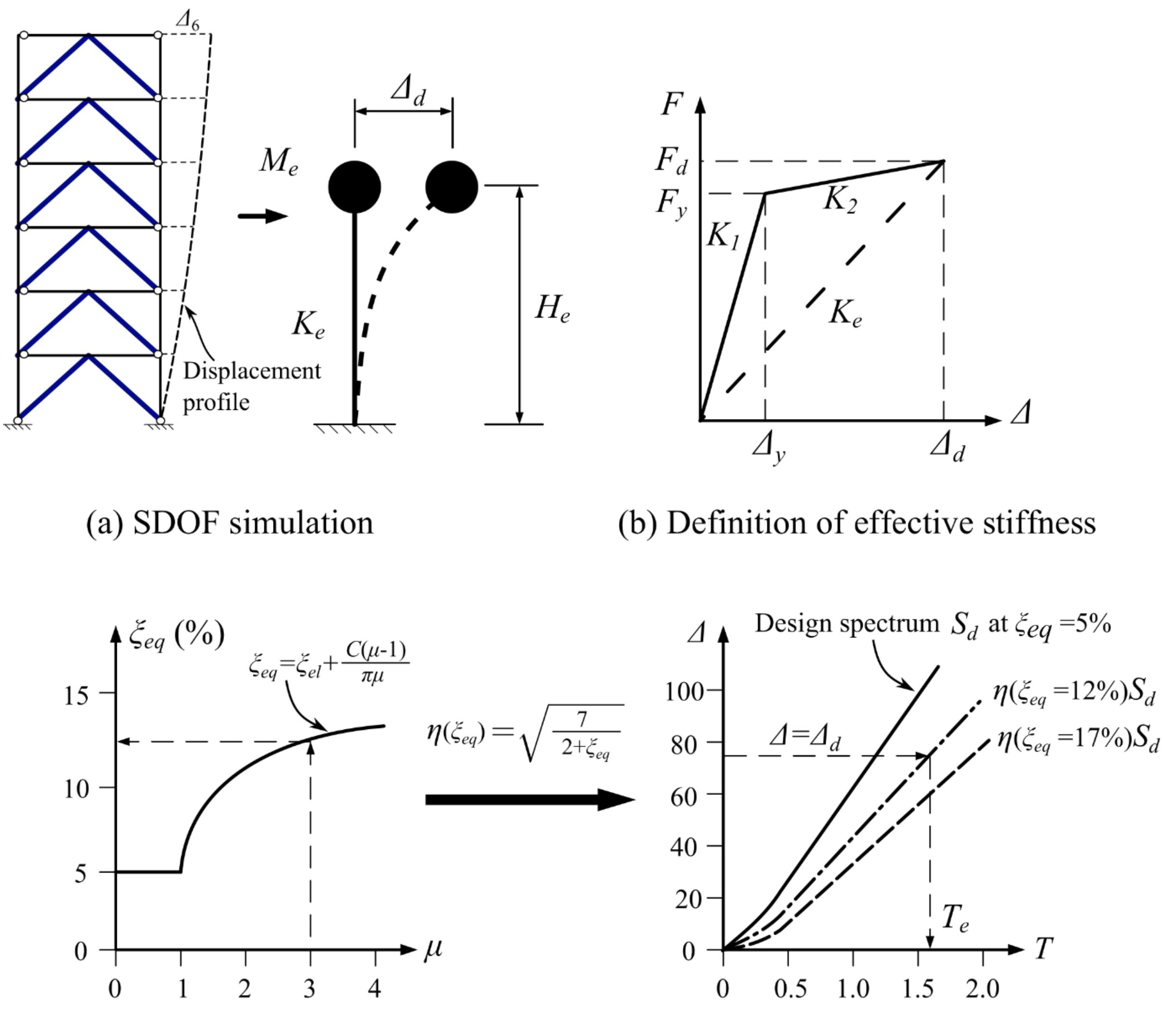

(a) SDOF simulation

(b) Definition of effective stiffness

(c) Equivalent viscous damping

(d) Design displacement spectra

Figure 3 DDBD design approach after Priestley et al. [17]

The second step is to calculate the equivalent SDOF system ductility demand μ at the design displacement Δ_d according to Eq. 4, with the design and yield displacement points shown in Figure 3b. To quantify the effects of nonlinear behaviour on the displacement demands, Priestley et al. [17] recommended characterising the equivalent SDOF system with an equivalent viscous damping ratio ξ_{eq}, which is a function of ductility factor μ, as shown in Figure 3c. ξ_{eq} is computed using an empirical ξ_{eq}-μ relationship calibrated to the results of

NLTHA, as will be discussed further in Section 3.3. The design displacement spectrum of an SDOF system is scaled to ξ_{eq}, as shown in Figure 3d, using the spectral displacement reduction factor η, a function of ξ_{eq}. Thus, the required T_e for the equivalent SDOF system can be obtained according to Δ_d. Then, K_e and the design base shear force V_d can be determined using Eq. 5 and Eq. 6, respectively, when the P-Δ effects are not significant.

$$\mu = \frac{\Delta_d}{\Delta_y} \qquad \text{Eq. 4}$$

$$K_e = (\frac{2\pi}{T_e})^2 M_e \qquad \text{Eq. 5}$$

$$V_d = K_e \Delta_e \qquad \text{Eq. 6}$$

The design base shear force V_d for the equivalent SDOF system is also the design base shear force for the MDOF structure, so the third step is to distribute V_d along the height of the structure as storey forces F_i using Eq. 7. These forces are used to design the structural members in MDOF structures, with possible adjustments to the force profile for taller buildings to mitigate higher mode effects (as clarified later in Section 3.2).

$$F_i = \frac{m_i \Delta_i}{\sum_{i=1}^{n} m_i \Delta_i} V_d \qquad \text{Eq. 7}$$

3 Extending the DDBD approach to the BRBGF structures

To apply the DDBD approach to BRBGF structures, the following knowledge is required: (1) the displacement profile and the design displacement at the performance limit state for BRBGF structures when substituting BRBGFs into an equivalent SDOF system (Figure 3a); (2) μ for the BRBGF structures (Figure 3c), requiring estimation of the yield displacement; and (3) the relationship between ξ_{eq} and μ to obtain T_e (Figure 3c and Figure 3d). In this section, the determination of these design parameters is discussed.

3.1 Displacement profile and limit state displacement

The design displacement Δ_d of the equivalent SDOF system depends on the assumed displacement profile and the limit state displacement of the MDOF structure, as shown in Eq. 1. Past research has shown that the empirical displacement profile for moment-resisting frame (MRF) structures proposed by Priestley et al. [17] is also suitable for concentrically braced frame (CBF) structures [48,49]. Rajeev et al. [47] verified the feasibility of the empirical displacement profile based on numerous NLTHAs of steel CBF structures; Maley et al. [23] also found that it worked well for dual BRB-MRF systems. Therefore, the empirical displacement profile shown in Figure 4 was used for BRBGF structures. The first storey has the largest inter-storey drift ratio, so the performance limit state displacement is governed by the first storey design inter-storey drift ratio θ_d. The empirical design displacement profile can be expressed as a function of θ_d as shown in Eq. 8a according to Sullivan et al. [47]. Suppose more accurate displacement profiles of multi-storey BRBGF structures from shake table testing or building monitoring are available in the future. In that case, the displacement profile assumption can be improved, but the entire process of the DDBD approach presented in this study could remain the same.

Previous research illustrated that higher mode effects might increase the peak storey drift demands [50]. Sullivan [24] suggested reducing the first mode design displacement profile to account for the additional displacements caused by the higher mode effects. Therefore, the design drift reduction factor ω_θ (Eq. 8b) adapted by Sullivan et al. [47] was included in the displacement profile to account for the higher mode effects of BRBGF structures.

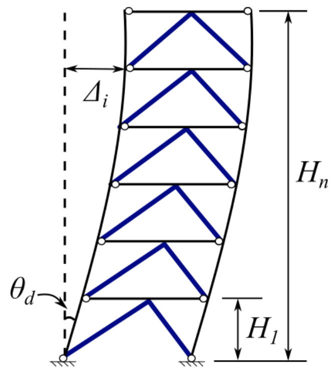

Figure 4 Assumed displacement profile

$$\Delta_i = \begin{cases} \theta_d H_i & n \le 4 \\ \omega_\theta \theta_d H_i \dfrac{(4H_n - H_i)}{(4H_n - H_1)} & n \ge 4 \end{cases} \quad \text{Eq. 8a}$$

$$\omega_\theta = \begin{cases} 1.0 & n \le 6 \\ 1 - 0.015(n-6) & 6 < n \le 16 \end{cases} \quad \text{Eq. 8b}$$

The design inter-storey drift ratio θ_d depends on the performance requirements of both structural and non-structural elements. Recent research on low-damage non-structural elements showed that the improved design of these non-structural elements could sustain a 2.0–2.5% drift ratio with minor damage [51]. As the performance limits of non-structural elements are out of the scope of this study, the performance limits were determined by the structural elements. The serviceability performance limit of θ_d was set to 0.33% based on New Zealand engineering practice [44]. The BRBGF tests [14] showed that the residual drift ratio could be over 0.5% after loading to a 1.0% drift ratio, and the residual drift ratio of 0.5% was suggested as the permissible residual drift ratio for safety by McCormick et al. [52], so the repairable damage limit state of θ_d was set to 1.0%. The ultimate limit state (ULS) drift ratio was set to 2.0% conservatively because the BRBGF tests [14] proved that the BRBGF structures could sustain this drift limit without collapse or significant damage in timber members and connections [14]. A higher θ_d may be adopted in the future if it is verified through further research and testing.

3.2 Ductility factor

The ductility factor μ of the equivalent SDOF system is used to estimate the equivalent viscous damping ξ_{eq}, as shown in Figure 3c, before obtaining the effective period T_e. The yield displacement Δ_y is required to determine μ, as shown in Eq. 4. The following sub-section discusses the determination of Δ_y and links the ductility factor of each storey of the BRBGF structure with its equivalent SDOF system.

3.2.1 Yield drift of one-storey BRBGFs

Numerical models of the one-storey BRBGFs were built, as shown in Figure 5. The experimental tests showed that the BRB-timber interface connections had negligible moment-resisting capacity [14], so their rotational stiffness was set to zero. The translational stiffness of the interface connections was modelled using *Pinching4* models in OpenSees with *ZeroLength* elements between nodes 5 and 6, nodes 1 and 7, and nodes 3 and 8. As shown in Figure 2, the initial slips were simulated by *ElasticMultiLinear* model in OpenSees as a spring in series between nodes 5 and 6. The stiffness of the *ElasticMultiLinear* model was low when the drift was smaller than the specified initial slips, but the stiffness would be significantly higher than that of BRBs when the drift exceeded the initial slips. The detailed parameters for the interface connections and the experimental verification process can be found in [16]. Several methods have been used to define the yield drift [17]. The definition from Park [53] was used here because it could include the influence of the initial slips that might exist in BRBGF structures. In addition, the two well-defined linear parts of the backbone curves of the BRBGF specimens fitted the definition well [14]. The yield drift, $\delta_{y,s}$, is defined as the lateral displacement corresponding to the yield strength, F_y, calculated using Eq. 9 and is equal to the lateral force when both BRBs yield. Pushover analyses were conducted for the one-storey BRBGFs with and without the initial slips; Figure 6 shows the load-drift curves. The curves illustrate that the yield drift with initial slips $\delta_{y,s}$ was the yield drift without initial slips $\delta_{y,0}$ plus initial slips δ_s, as shown in Eq. 10.

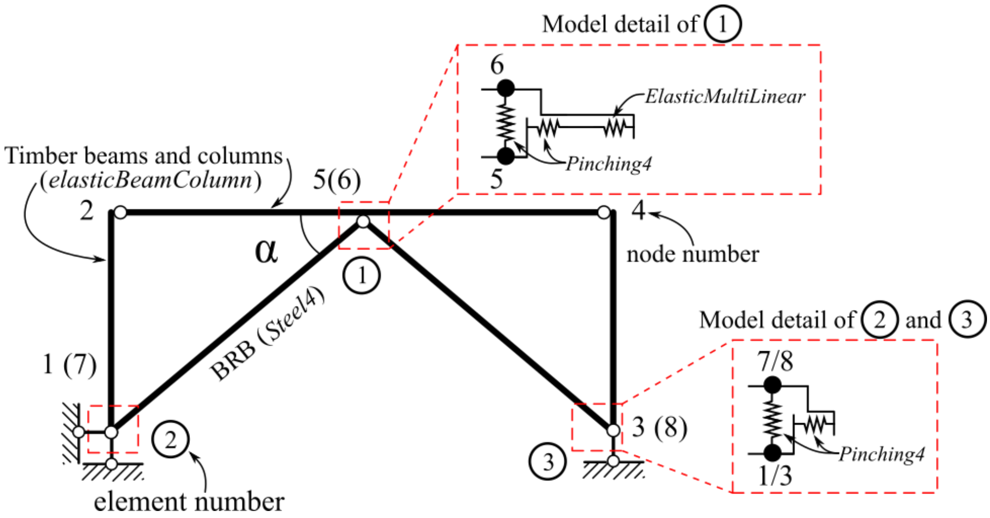

Figure 5 Numerical model of the one-storey BRBGF

$$F_y = 2\phi_m f_y A_c cos\alpha \quad \text{Eq. 9}$$

$$\delta_{y,s} = \delta_{y,0} + \delta_s \quad \text{Eq. 10}$$

where ϕ_m is the material overstrength factor for the steel core of BRB; f_y is the expected steel yield strength (MPa); A_c is the area of the yield zone of steel core of BRB (mm^2), and α is the inclination angle of the BRBs as shown in Figure 5.

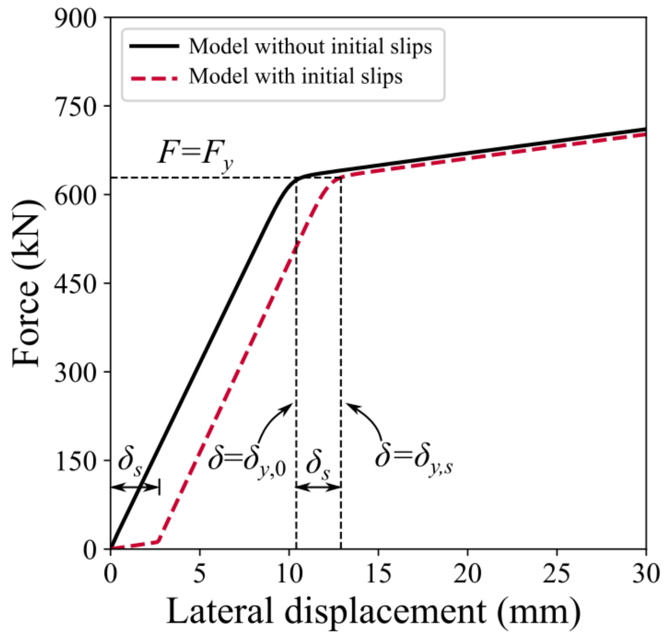

Figure 6 Yield drift definition

3.2.2 Yield drift of multi-storey BRBGFs

Past research [23,47,49,54] has illustrated that the inter-storey yield drift at the *i*-th storey $\delta_{y,i}$ in a multi-storey building may need to consider the inter-storey drift caused by the BRB deformation $\delta_{y,i,BRB}$, and the inter-storey drift caused by the column axial deformation $\delta_{y,i,col}$, as shown in Figure 7. Similar to the one-storey BRBGF, the inter-storey drift contributions of the initial slips $\delta_{s,i}$ need to be included, so $\delta_{y,i}$ was calculated using Eq. 11.

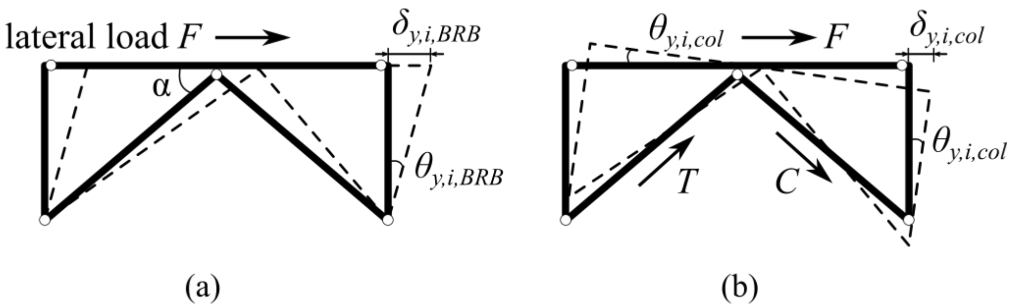

Figure 7 Yield drift components (a) the drift contribution of the BRB deformation $\Delta_{y,i,BRB}$; (b) the drift contribution of the column axial deformation $\Delta_{y,i,col}$

$$\delta_{y,i} = \delta_{y,i,BRB} + \delta_{y,i,col} + \delta_{s,i} \qquad \text{Eq. 11}$$

The component $\delta_{y,i,BRB}$ was estimated using Eq. 12a based on Sullivan et al. [47]. In BRB steel frames, the connections between BRBs and steel frames are usually translationally rigid. The frame lateral stiffness is equal to the lateral stiffness of BRBs, whereas, in BRBGF structures, the connection stiffness should be considered. Stiffness is considered by introducing a stiffness adjustment factor λ, as shown in Eq. 12b. λ defines the lateral stiffness ratio between the BRBGF with translationally semi-rigid dowelled connections and the BRBGF with translationally rigid connections; therefore, λ should be between 0 and 1. The BRBs were modelled by *Steel4* model in OpenSees as a truss, as shown in Figure 5; thus the stiffness of BRBs was represented by an effective stiffness, $K_{eff,BRB}$, as shown in Eq. 13a dependent on the geometry of the yield zone, transition zone and elastic zone of BRBs according to Vigh and Zsarnóczay [55]. To simplify the calculation, the additional stiffness caused by the transition zone and the elastic zone was considered by a stiffness modification factor f_{sm} that amplified the elastic modulus of steel core E_s as shown in Eq. 13b according to Vigh and Zsarnóczay [55]. The detailed parameters for *Steel4* can be found in the Appendix of [16]. In terms of that, the yield strain ε_y in Eq. 12a was calculated using Eq. 12c to include the influence of steel core material (f_y, ϕ_m, and E_s) and BRB geometry (f_{sm}).

$$\delta_{y,i,BRB} = h_i \theta_{y,i,BRB} = h_i \frac{2\varepsilon_y}{\lambda sin 2\alpha} \qquad \text{Eq. 12a}$$

with

$$\lambda = \frac{k_{BRBGF}}{k_{BRBGF,rigid}} \qquad \text{Eq. 12b}$$

$$\varepsilon_y = \frac{\phi_m f_y}{f_{sm} E_s} \qquad \text{Eq. 12c}$$

where h_i is the storey height of the i-th storey (m); and $\theta_{y,i,BRB}$ is the inter-storey drift ratio of the i-th storey caused by BRB deformations; ε_y is the BRB yield strain; f_{sm} is the stiffness modification factor as defined in Eq. 13; and E_s is the elastic modulus of steel core (GPa).

$$K_{eff,BRB} = E_s \frac{A_c A_{tr} A_e}{A_c A_{tr} l_e + A_c A_e l_{tr} + A_{tr} A_e l_c} = E_s f_{sm} \frac{A_c}{l_{wp}} \qquad \text{Eq. 13a}$$

$$E_{eff,BRB} = f_{sm} E_s \qquad \text{Eq. 13b}$$

$$l_{wp} = l_e + l_{tr} + l_c \qquad \text{Eq. 13c}$$

where $K_{eff,BRB}$ is the BRB effective stiffness (kN/mm); A_c, A_{tr}, and A_e are the area (mm^2) of the yield zone, transition zone and elastic zone of the BRB, respectively; l_c, l_{tr}, and l_e are their corresponding length (mm) [56]; and f_y is the expected steel yield strength.

Figure 8 shows a spring analogy model for the BRBGF, similar to the model proposed by Mahjoubi and Maleki [57]. As the top connection carried the load approximately twice as much as the bottom connections in the BRBGFs, the fastener number in the bottom connections was assumed to be half of that of the top connections. In this regard, the translational stiffness of the bottom connection $k_{con,b}$ was approximately half of that of the top connections $k_{con.t}$ in the model (i.e., $k_{con.t} = 2k_{con.b}$). To simplify the spring analogy model further, a stiffness ratio v between $k_{con,b}$ and the BRB lateral stiffness $k_{BRBGF,rigid}$ is defined as Eq. 14a. $k_{BRBGF,rigid}$ represents the BRBGF stiffness with the assumption of translationally rigid connections; k_{BRBGF} can be calculated using Eq. 14b considering the contributions from the translationally semi-rigid top and bottom connections. By comparing Eq. 12b and Eq. 14b, λ is a function of v, as shown in Eq. 14c.

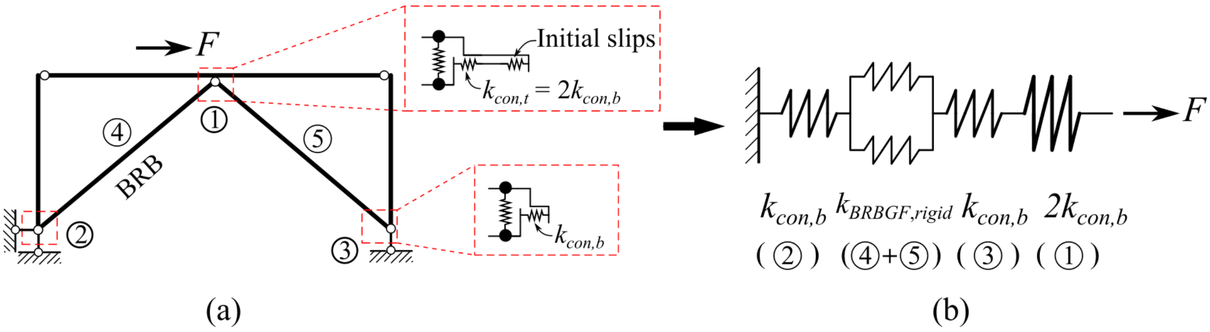

Figure 8 BRBGF spring analogy

$$v = \frac{k_{con,b}}{k_{BRBGF,rigid}} \qquad \text{Eq. 14a}$$

$$\frac{1}{k_{BRBGF}} = \frac{2}{k_{con,b}} + \frac{1}{2k_{con,b}} + \frac{1}{k_{BRBGF,rigid}} = \left(\frac{2v+5}{2v}\right)\frac{1}{k_{BRBGF,rigid}} \qquad \text{Eq. 14b}$$

$$\lambda = \frac{2v}{2v+5} \qquad \text{Eq. 14c}$$

The component $\delta_{y,i,col}$ was calculated using Eq. 15a assuming that the columns exhibit similar deformations in tension and compression [49]. As it is difficult to determine the timber column strain before choosing the member sizes for BRBs, beams and columns, a strain adjustment factor ρ was used to convert the axial strain of timber column ε_{col} to the yield strain of yield zone of BRB ε_y, as shown in Eq. 15a. An average strain adjustment factor ρ_{avg} along the entire height was empirically assumed as 0.4 to simplify the preliminary design. This value is verified by NLTHA in Section 4.

$$\delta_{y,i,col} = h_i\theta_{y,i,col} = h_i\frac{2\sum_{j=1}^{i-1}\varepsilon_{col,j}h_j}{L} = 2h_i\varepsilon_y\frac{\sum_{j=1}^{i-1}\rho_j h_j}{L} = 2h_i\varepsilon_y\rho_{avg}\frac{\sum_{j=1}^{i-1}h_j}{L} \qquad \text{Eq. 15a}$$

$$\rho_j = f_{sm} E_s \frac{\sum_{k=j+1}^{k=n} A_{c,k} sin\alpha}{A_{col,j} E_{GL}} \qquad \text{Eq. 15b}$$

where $\varepsilon_{col,j}$ is the axial strain of glulam columns at the j-th storey below the i-th storey (i.e. $j < i$); ρ_j is the strain adjustment factor between the glulam columns and BRB at the j-th storey; L (= 8 m) is the span of BRBGF; $A_{c,k}$ (mm^2) is the BRB yield zone area at the k-th storey above the j-th storey (i.e. $j < k < n$); E_{GL} (= 10 GPa) is the glulam column elastic modulus; and $A_{col,j}$ is the glulam column cross-section area (mm^2) at the j-th storey.

3.2.3 Ductility factor of the equivalent SDOF system μ_{sys}

The ductility factor of the equivalent SDOF system μ_{sys} is defined by Eq. 16a according to Maley et al. [23]. Similar to Eq. 4, the ductility factor for the i-th storey μ_i is defined by Eq. 16b. Although the base shear force V_{base} is initially unknown, Eq. 16a contains the shear force in the numerator and denominator. For the initial design, μ_{sys} can be obtained by assuming a total base shear V_{base} = 1.0 and recognising that the strength proportions are a design choice. The shear force at the i-th storey V_i was calculated using Eq. 16c. Different from Eq. 7, Sullivan et al. [47] recommended Eq. 16d to distribute the base shear force over the height of frame systems, where an additional 10% of the base shear force was allocated at the roof level to consider the higher mode effects.

$$\mu_{sys} = \frac{\sum_{i=1}^{n} V_i \Delta_i \mu_i}{\sum_{i=1}^{n} V_i \Delta_i} \qquad \text{Eq. 16a}$$

$$\mu_i = \frac{(\Delta_i - \Delta_{i-1})}{\delta_{y,i}} \qquad \text{Eq. 16b}$$

$$V_i = \sum_{j=i}^{n} F_j \qquad \text{Eq. 16c}$$

where, F_j is the distributed load at the j-th storey:

$$F_j = \begin{cases} 0.9 \dfrac{m_j \Delta_j}{\sum_{i=1}^{n} m_i \Delta_i} V_{base} & j < n \\ \left(0.1 + 0.9 \dfrac{m_n \Delta_n}{\sum_{i=1}^{n} m_i \Delta_i}\right) V_{base} & j = n \end{cases} \qquad \text{Eq. 16d}$$

3.3 Equivalent viscous damping ξ_{eq} and spectral displacement reduction factor η

The Relationships among the ductility factor μ, equivalent viscous damping ξ_{eq}, and spectral displacement reduction factor η of the equivalent SDOF system are required for the DDBD approach, as shown in Figure 3c and Figure 3d. ξ_{eq} has traditionally been calculated by Eq. 17 as the summation of elastic viscous damping ξ_{el} and hysteretic damping ξ_{hyst}. Traditionally, ξ_{hyst} has been calculated using Eq. 18a based on an area-based approach proposed by Jacobsen [58]. However, several studies have indicated that the area-based approach can be inaccurate, especially for systems with a high energy dissipation capacity [59,60]. As such, ξ_{hyst} was calibrated using the results of NLTHA and Eq. 18b for different types of hysteretic models [59,61,62] and structures [24,63–71] including timber-steel hybrid structures [72] and BRB steel frames [47]. Even though expressions for timber and BRB systems exist, the hysteretic behaviour of BRBGFs is different from that of other timber-steel hybrid structures. In addition, ξ_{hyst} for BRB steel frames was derived by using the bi-linear hysteretic shape for BRBs [47], which might not accurately represent the performance of BRBs because the isotropic and kinematic hardening in tension and compression could be significant [55] and the initial slips and semi-rigid connections in BRBGFs might reduce ξ_{hyst}.

$$\xi_{eq} = \xi_{el} + \xi_{hyst} \qquad \text{Eq. 17}$$

$$\xi_{hyst} = \frac{1}{2\pi}\frac{A_{hyst}}{F_m \Delta_m} \qquad \text{Eq. 18a}$$

$$\xi_{hyst} = \frac{C(\mu - 1)}{\pi\mu} \qquad \text{Eq. 18b}$$

where, A_{hyst} is the dissipated energy in an entire hysteretic loop (kJ); F_m and Δ_m are the maximum force (kN) and displacement (mm) for the hysteretic loop, respectively; and C is a constant.

In addition to the ductility-dependent equivalent viscous damping expression, an expression is required to scale displacement spectra to different levels of equivalent viscous damping. Eq. 19a and Eq. 19b provide equations for the spectral displacement reduction factor η in the previous Eurocode 8 [73] and current Eurocode 8 [21]. This factor is used to scale the displacement spectrum based on ξ_{eq} and then obtain the required effective period T_e, as shown in Figure 3d. However, past research [60,74] has demonstrated that the ξ_{eq}-μ relationship is dependent on site seismicity, and this dependency is not explicitly expressed in Eq. 18b. Using Eq. 18b with Eq. 19a and Eq. 19b may result in inconsistent designs at different sites [74]. Therefore, Pennucci et al. [74] suggested combining the two steps in Figure 3c and Figure 3d into one step and deriving the relationship between η and μ directly because the η-μ relationship did not show an apparent dependency on the site seismicity. A more detailed explanation on using the form of Eq. 20 over Eq. 19 can be found in [75]. Improved accuracy was observed from numerous NLTHAs by Pennucci et al. [74]. In this study, an attempt was made to establish a direct relationship between η and μ for the BRBGF structures.

$$\eta_1 = \sqrt{\frac{7}{2 + \xi_{eq}}} \quad \text{Eq. 19a}$$

$$\eta_2 = \sqrt{\frac{10}{5 + \xi_{eq}}} \quad \text{Eq. 19b}$$

Figure 9 shows the comparison between the numerical modelling results of the BRBGF with dowelled connections in Figure 2 and the fitted Takeda fat hysteresis model (r_t = 0.05, β_t = 0.6 and D = 0.0) in Figure 10. Although the Takeda fat model is often used to represent the hysteresis loops of concrete frames [17], the comparison shows that it can also provide an approximate fit to the hysteresis loops of the BRBGF. The maximum difference of the total energy dissipation was about 10% (291 kJ versus 261 kJ). The η-μ relationship for the Takeda fat model, given by Eq. 20, was calibrated by Pennucci et al. [74] with numerous NLTHAs. In this study, we determined whether Eq. 20 can also be applied to BRBGF structures.

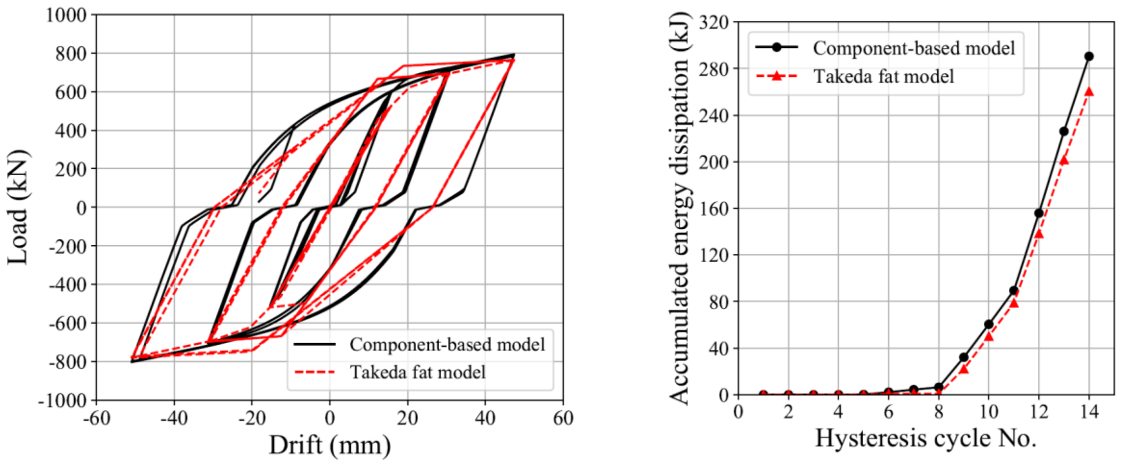

(a) Hysteresis loops

(b) Accumulated energy dissipation

Figure 9 Comparison between the component-based model and Takeda fat model

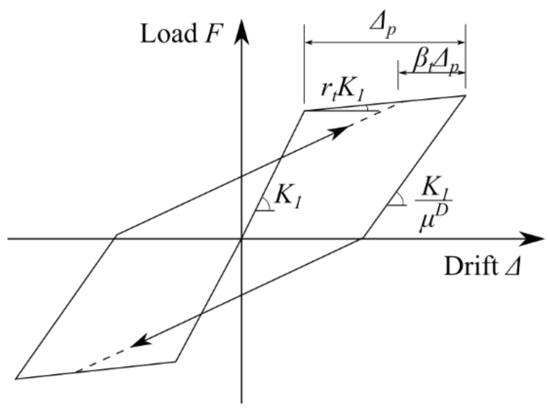

Figure 10 Takeda fat model [17]

$$\eta_3 = \sqrt{\frac{\pi\mu}{11.04\mu - 7.9}} \qquad \text{Eq. 20}$$

3.4 Calibration of design parameters

The stiffness adjustment factor, λ (Eq. 12b) must be determined and the applicability of the η-μ relationship (Eq. 20) for BRBGF structures must also be assessed. Pushover analyses and NLTHAs were conducted to determine λ and assess Eq. 20, respectively, using numerical models of the one-storey BRBGF as shown in Figure 5.

3.4.1 Numerical models

A series of one-storey BRBGF models were built in OpenSees. The models had an 8 m span and 3.6 m height with BRBs installed at an inclination angle α = 42°. All BRBs were made of S235 [76] steel with a material overstrength ϕ_m = 1.2 [47], elastic modulus E_s = 210 GPa and a BRB overstrength factor γ_{BRB} = 1.5, i.e., $\omega\beta$ = 1.5, where ω is the BRB strain hardening adjustment factor, and β is the BRB compression strength adjustment factor [77]. Three design variables were considered: (1) cross-section of the yield zone in BRBs, (2) stiffness modification factor f_{sm}, and (3) initial slips due to manufacturing tolerances. Table 1 lists the configurations of the BRBGFs considered. Three cross-sections of BRBs were considered for implementation in the lower, middle and upper storeys of a BRBGF structure [14], which corresponded to a lateral design load of 226 kN, 436 kN and 629 kN, respectively. The BRBGF yield load was calculated by Eq. 9. All connections were designed with a connection relative overstrength factor $\gamma = \gamma_{BRB}$ = 1.5, i.e., the design strength of the connections was 1.5 times the load transferred to the connections when the BRBs yielded [16]. Although f_{sm} depends on the BRB geometry [78], it typically varies within ± 10% if the same steel grade is used. In this regard, three different values of f_{sm} were included to consider the influence of BRB stiffness. In addition, three different levels of initial slips caused by manufacturing tolerances were considered for ideally tight, medium and maximum allowable manufacturing tolerances in practice [16]. Thus, 27 BRBGF configurations were considered in the simulations; each of them was denoted according to the combination of design variables. For example, "75 × 20-1.22-2.5" represents a BRBGF with 75 mm × 20 mm yield zone of BRBs, f_{sm} = 1.22, and ± 2.5 mm initial slips.

Table 1 Parameters of one-storey BRBGF models

Cross-section of yield zone (mm×mm)	f_{sm}	Initial slips (± mm)
45 × 12	1.10	0.0
65 × 16	1.22	2.5
75 × 20	1.34	4.0

3.4.2 Analyses of one-storey BRBGF models

Following the procedure shown in Figure 11, numerical simulations were conducted on the 27 BRBGF configurations. Pushover analyses were performed first and the system and component stiffness values were evaluated. Table 2 lists the results for λ which are between 0.70 and 0.74. Therefore, the average λ = 0.72 is used in Eq. 12a to calculate the BRBGF drift $\delta_{y,i,BRB}$ when the BRBs begin to yield. λ = 0.72 also means that the translationally semi-rigid dowelled connections between the BRBs and glulam frames causes a 28% reduction in the system stiffness compared with the BRBGF with the translationally rigid connection assumption.

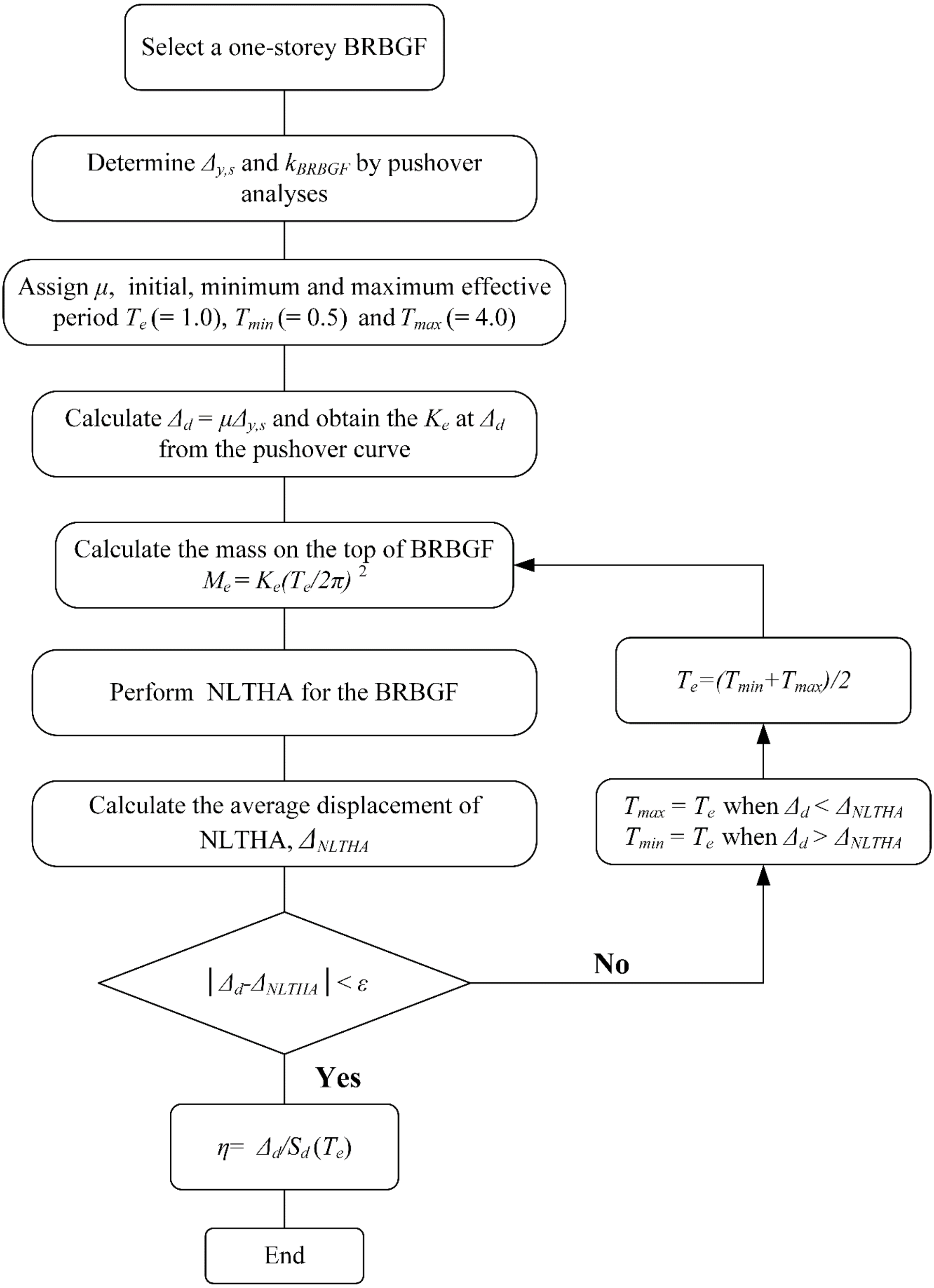

Figure 11 Procedure of parameter verification

Table 2 Results of stiffness adjustment factor λ

BRB cross-section	45 × 12			65 × 16			75 × 20		
f_{sm}	1.10	1.22	1.34	1.10	1.22	1.34	1.10	1.22	1.34
λ	0.74	0.72	0.70	0.74	0.71	0.70	0.74	0.72	0.70

NLTHA was then conducted using ten ground motion records selected by Maley et al. [79] from the Pacific Earthquake Engineering Research Centre database [80] and GeoNet [81], as listed in Table 3. The near-fault effect was not considered in the records. The average acceleration spectra were scaled to match the design acceleration spectra of soil type D in New Zealand seismic load standard NZS 1170.5 [22]. The average acceleration spectra were scaled to an intensity level of 0.23g with a return period of 25 years, as shown in Figure 12, ensuring that T_e of the equivalent SDOF system mostly fell into the $T_e > 1.0$ s region. Research by Dwairi et al. [59] and Grant et al. [60] has shown that η is lower for $T_e < 1.0$ s than that for $T_e > 1.0$ s. Additionally, T_e for most structures falls into the $T_e > 1.0$ s region [17], so scaling into $T_e > 1.0$ s region will result in more realistic predictions for most structures. The scale factors are denoted as SF1 in Table 3. The design acceleration spectrum $S_a(T)$ in Figure 12 are transferred to the design displacement spectrum $S_d(T)$ using Eq. 21 to calculate η.

Table 3 Ground motion records and scale factors for NLTHA

No.	Event	Station	RSN	Component	Magnitude	V_{s30} (m/s)	SF1	SF2
1	Chi-Chi	TAP042	1430	E	7.62	273	0.71	2.92
2	Landers	Desert Hot Springs	850	090	7.28	345	0.86	3.00
3	Hector	USGS 5295 North Palm Springs Fire Sta #36	1816	270	7.13	345	1.35	5.51
4	Darfield	Westerfield (WSFC)	-*	N00E	7.10	-	1.90	7.23
5	Loma Prieta	CDMG 47179 Salinas-John & Work	800	160	6.93	271	1.08	4.72
6	Kobe	OSAJ	1113	090	6.90	256	0.77	3.43
7	Superstition Hills-02	USGS 5210 Wildlife	729	090	6.54	208	0.41	1.89
8	Imperial Valley-06	Delta	169	352	6.53	275	0.40	1.47
9	Chi-Chi Taiwan-03	CHY055	2477	W	6.20	226	1.54	6.65

10	Chalfant Valley-02	CDMG 54171 Bishop-LADWP South St	549	180	6.19	271	0.83	3.02

*Note: from GeoNet database (https://www.geonet.org.nz/)

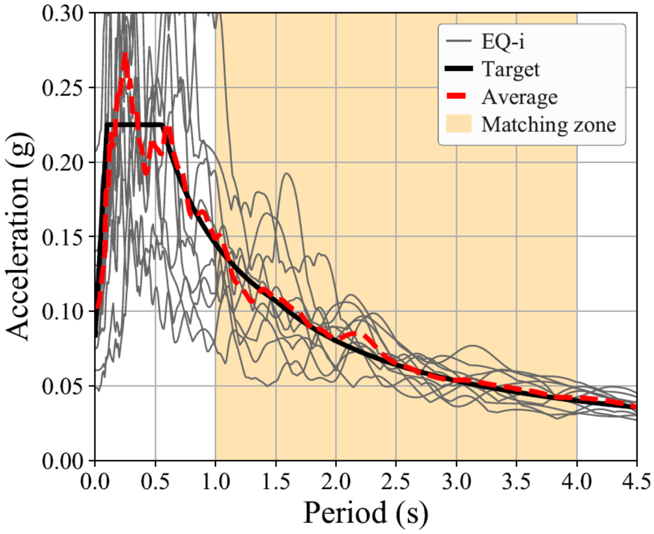

Figure 12 Acceleration spectra scaling process

$$S_d(T) = \left(\frac{T}{2\pi}\right)^2 S_a(T) \qquad \text{Eq. 21}$$

The NLTHA was conducted for each one-storey BRBGF model from μ = 1.5 to 6.0 with an increment of 0.5, resulting in 270 equivalent SDOF systems. 27 of them fell outside the matching zone in Figure 12 and were discarded. The 243 remaining equivalent SDOF systems were used to calculate η by Eq. 22. The three variables in Table 1 had a minor influence on the η–μ relationship. For example, the results of η from equivalent SDOF systems with different initial slips are plotted with different symbols in Figure 13 and no significant difference was observed among them. The reason might be that these variables primarily affected the magnitude of the yield drift $\delta_{y,s}$, while μ included the influence of $\delta_{y,s}$. Figure 13 shows that the best-fitted curve from the 243 equivalent SDOF systems (denoted as η_4) was similar to η_3 for the Takeda fat model and slightly smaller than η_3, that is, on the conservative side. This agrees with the earlier observation in Figure 9 that the Takeda fat model tends to slightly underestimate the energy dissipated by BRBGF structures at large displacements.

Therefore, η_3 (Eq. 20) can be used to represent the spectral displacement reduction factor for BRBGF structures conservatively.

$$\eta = \frac{\Delta_d}{S_d(T_e)} \qquad \text{Eq. 22}$$

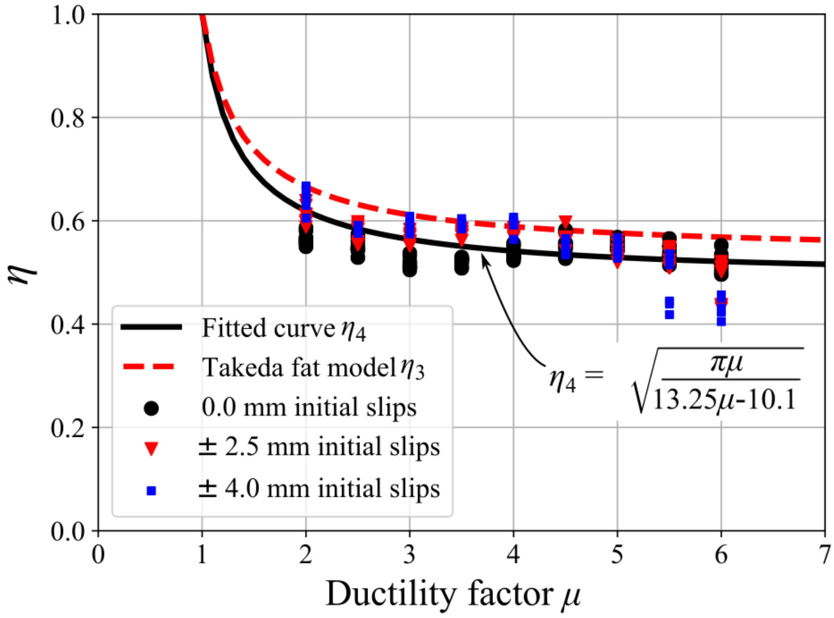

Figure 13 Verification of η-μ relationship

4 Case studies on the DDBD approach

The DDBD approach with calibrated parameters was used for the ULS seismic design of case study BRBGF buildings with three, six, and nine storeys. Numerical models of these buildings were established in OpenSees and analysed using real earthquake ground motion records. The analysis results were compared with design values to verify the DDBD approach.

4.1 Case study buildings

The three BRBGF buildings with three, six and nine storeys were denoted as BRBGF-3, BRBGF-6, and BRBGF-9, respectively. They shared the same floor plans, and BRBGF-6 is shown in Figure 14 as an example. These buildings are located in Christchurch, New Zealand. Continuous glulam columns for every three storeys were used to reduce splice joints of columns and for transportation convenience, which is also a common practice for timber construction. CLT floors and roofs with concrete topping were used with a rigid diaphragm assumption. The weights of the floors and roof were obtained from the CLT manufacturer [82] and all the loading information is listed in Table 4 according to NZS 1170.5 [22]. Appendix I provides a design flowchart of the procedure of extended DDBD approach mentioned in Section 3.

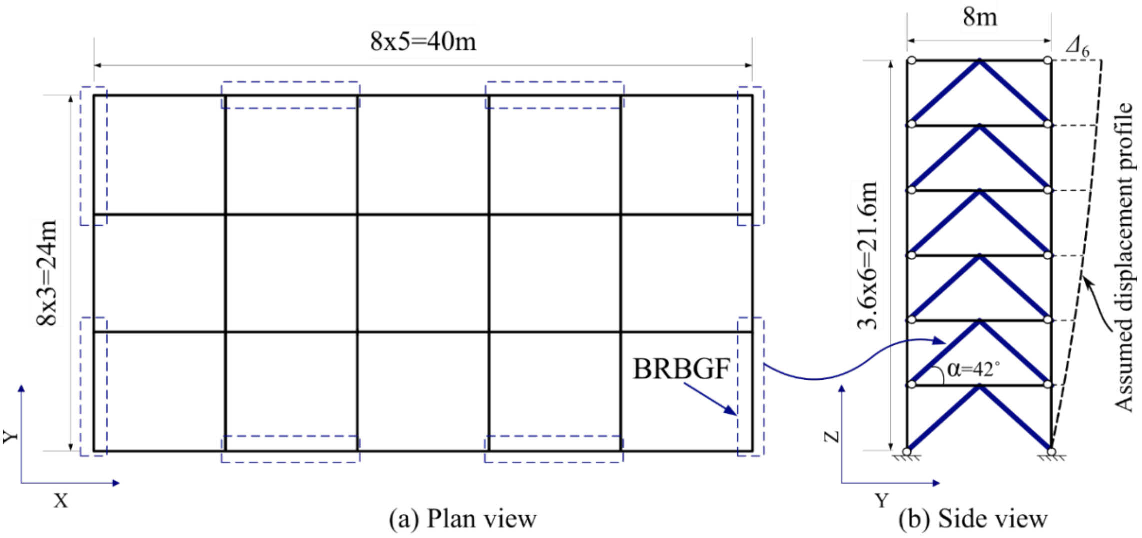

Figure 14 BRBGF-6 design example

Table 4 Loading information of case study buildings

Item	Value	Item	Value
Importance level	2	Return period factor *R*	1.0
Design working life	50 years	Near-fault factor *N*	1.0
Annual probability of exceedance	1/500	Dead load on floor	1.8 kPa
Site subsoil class	D	Dead load on roof	1.6 kPa
Hazard factor *Z*	0.3	Live load on floor	3.0 kPa

4.2 Design results of the DDBD approach

The design information for BRBGF-6 is listed in Table 5 as an example. Appendix II shows a detailed step-by-step procedure for parameters in Table 5. The elastic viscous damping ξ_{el} was assumed to be 2% [44]. Pennucci et al. [74] proposed Eq. 23a that uses $\gamma_{2\%}$ to adjust η_3 from ξ_{el} = 5% to ξ_{el} = 2% ,which is denoted as $\eta_{\xi=2\%}$. The corresponding design displacement spectrum at ξ_{el} = 2% (denoted as $S_{d,2\%}$ (T)) was first obtained using η_2 according to Eurocode 8 [21], as shown in Eq. 23c, and then reduced by $\eta_{\xi=2\%}$ to obtain T_e, as shown in Figure 15.

Subquently, K_e and V_d were calculated using Eq. 5 and Eq. 6, respectively. Furthermore, the design base shear V_{base} should include the P–Δ effects using Eq. 24 according to Sullivan et al. [47].

Table 5 Design parameters of BRBGF-6

Storey	h_i	H_i	m_i (ton)	Δ_i (mm)	$\delta_{y,i,BRB}$ (mm)	$\delta_{y,i,col}$ (mm)	δ_s (mm)	$\delta_{y,i}$ (mm)	μ_i	V_i	F_i (kN)
1	3.6	3.6	65.6	72.0	11.1	0.0	2.5	13.6	5.3	1.00	31
2	3.6	7.2	65.6	137.7	11.1	1.7	2.5	15.3	4.3	0.94	59
3	3.6	10.8	65.6	197.2	11.1	3.5	2.5	17.0	3.5	0.84	84
4	3.6	14.4	65.6	250.4	11.1	5.2	2.5	18.8	2.8	0.68	107
5	3.6	18	65.6	297.4	11.1	7.0	2.5	20.5	2.3	0.49	127
6	3.6	21.6	39.0	338.1	11.1	8.7	2.5	22.3	1.8	0.25	138

$$\eta_{\xi=2\%} = \frac{\Delta_d}{S_{d,2\%}(T)} = \gamma_{2\%}\eta_3 = 0.83 \times 0.59 = 0.49 \qquad \text{Eq. 23a}$$

$$\gamma_{2\%} = \left(1 - 0.25\frac{5\% - \xi_{el}}{5\%}\right)^{1.5\frac{\mu-1}{\mu}} = 0.83 \qquad \text{Eq. 23b}$$

$$S_{d,2\%}(T) = \eta_2 S_d(T) = \sqrt{\frac{10}{5 + \xi_{el}}}\, S_d(T) \qquad \text{Eq. 23c}$$

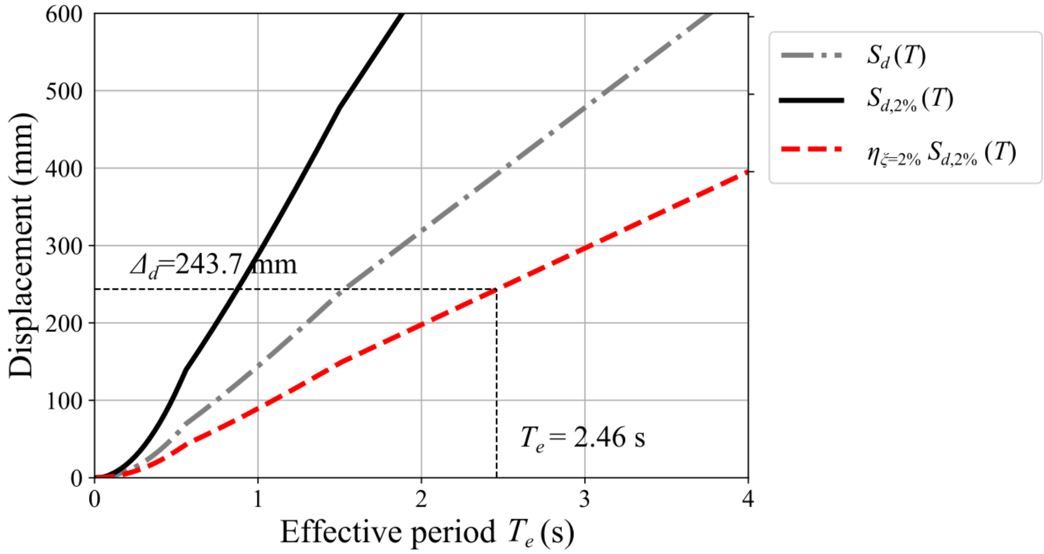

Figure 15 Adjusted displacement spectrum

$$V_{base} = V_d + V_{P-\Delta} \qquad \text{Eq. 24a}$$

$$V_{P-\Delta} = C_{P-\Delta} \frac{\sum_{i=1}^{n} m_i \, g \Delta_i}{H_{eff}} \quad \text{Eq. 24c}$$

$$C_{P-\Delta} = \begin{cases} 0.0 & \dfrac{M_{eff}\, g}{K_{eff} H_{eff}} < 0.05 \\ 1.0 & \dfrac{M_{eff}\, g}{K_{eff} H_{eff}} \geq 0.05 \end{cases} \quad \text{Eq. 24d}$$

where $V_{P\text{-}\Delta}$ is the additional base shear owing to the *P–Δ* effects; $C_{P\text{-}\Delta}$ is the *P–Δ* force adjustment factor; and g (= 9.8 m/s^2) is the gravitational acceleration.

A similar process was conducted for BRBGF-3 and BRBGF-9, and the design information of the three BRBGF structures is listed in Table 6.

Table 6 DDBD information of case study buildings

Parameters	BRBGF-3	BRBGF-6	BRBGF-9
Δ_d (mm)	132.4	243.7	341.1
M_e (ton)	151	310	466
H_e (m)	7.6	14.4	21.4
μ_{sys}	4.5	3.9	3.4
$\eta_{\xi=2\%}$	0.48	0.49	0.50
T_e (s)	1.38	2.46	3.4
V_{base} (kN)	441	544	622

4.3 Design BRB and glulam members

The base shear V_{base} was distributed over the height according to Eq. 16d. The shear force at the i-th storey V_i was resisted by two BRBs together, so the BRBs were designed using Eq. 25a and Eq. 25b according to the force equilibrium. Subsequently, glulam beams and columns were designed considering the BRB overstrength factor γ_{BRB} (= 1.5). The glulam columns were designed using the maximum axial load. The glulam beams were designed by combining the maximum axial load and corresponding moment caused by the uneven force of the two BRBs at the mid-span [83]. The member sizes of the three BRBGF structures are listed in Table 7-Table 9.

$$A_{c,i} = \frac{N_{i,BRB}}{\phi_m f_y} \quad \text{Eq. 25a}$$

$$N_{i,BRB} = \frac{V_i}{2cos\alpha} \qquad \text{Eq. 25b}$$

where $A_{c,i}$ is the yield zone area of BRB at the i-th storey (mm^2); and $N_{i,BRB}$ is the BRB axial load caused by V_i at the i-th storey (kN).

Table 7 Member size information of BRBGF-3

Storey	BRB cross section (mm)	Middle span connection ($n_r \times n_c$)	Beam (mm)	Column (mm)
1	12×79	3×8	360×315	
2	12×64	4×5	360×270	315×315
3	8×51	2×5	360×270	

Table 8 Member size information of BRBGF-6

Storey	BRB cross section (mm)	Middle span connection ($n_r \times n_c$)	Beam (mm)	Column (mm)
1	16×82	4×8	405×315	
2	16×77	5×6	405×315	360×360
3	16×68	4×7	405×270	
4	12×74	3×8	405×270	
5	12×53	3×5	315×270	270×270
6	8×42	3×3	315×270	

Table 9 Member size information of BRBGF-9

Storey	BRB cross section (mm)	Middle span connection ($n_r \times n_c$)	Beam (mm)	Column (mm)
1	20×74	6×6	450×315	
2	20×72	5×7	450×315	540×540
3	20×69	5×7	405×315	
4	20×63	4×8	405×315	
5	16×70	4×7	405×270	405×405
6	12×80	3×8	405×270	
7	12×64	3×6	405×270	
8	8×69	3×5	315×225	270×270
9	8×39	3×3	315×225	

4.4 Verification by NLTHA

4.4.1 Multi-storey BRBGF models

The DDBD approach was verified using NLTHA in OpenSees. The rigid diaphragm assumption was applied, so the seismic load was assumed to be equally distributed among the four BRBGFs in each direction of the buildings. For simplification, only one bay of the BRBGF structures was modelled and the gravity frames were simulated as a leaning column, as shown in Figure 16, with the BRBGF-6 model as an example. One-fourth of the seismic weight of the entire building was concentrated and added to the top of each storey as shown in Figure 16. The total seismic weight m_{total} were allocated to the BRBGF and the gravity frames according to their tributary areas. The seismic weight of floors and roofs in BRBGFs were calculated using Eq. 26 according to NZS 1170.5 [22] and the load information in Table 4. The tributary area $A_{tributary}$ in the X-direction of Figure 14 was 32 m^2 which came up with the seismic weight on floor node $m_{f,f}$ (= 8.7 tons) and roof node $m_{r,f}$ (= 5.1 tons) for the BRBGFs. The remaining m_{total} were added to gravity frames, modelled as a leaning column. The seismic weights on floor and roof node were $m_{f,l}$ (= 48.1 tons) and $m_{r,l}$ (= 27.8 tons), respectively.

$$S_{d,earthquake} = (G + \varphi_E Q)A_{tributary} \qquad \text{Eq. 26}$$

where $S_{d,earthquake}$ is the seismic weight (kN); G and Q are the dead load, and live load (kPa), respectively; and $A_{tributary}$ is the corresponding tributary area (m^2).

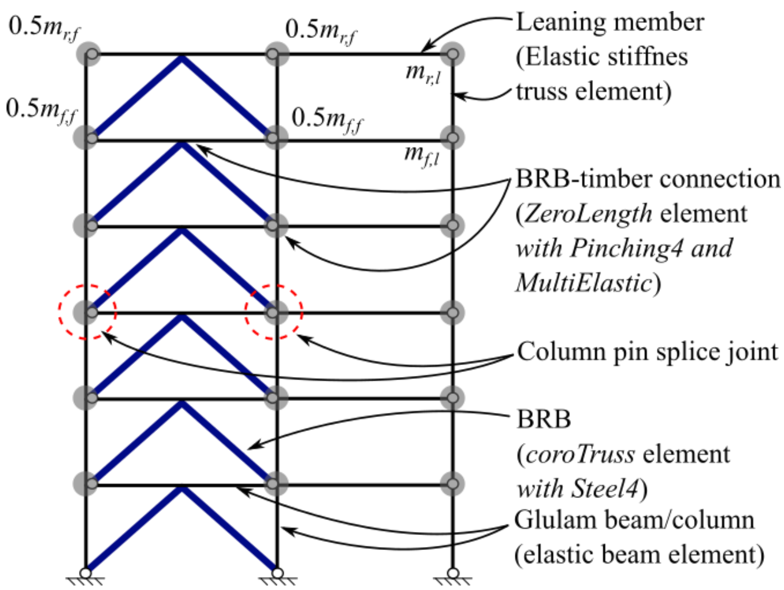

Figure 16 Six-storey BRBGF OpenSees model

The damping model from Lee [84–86] was used for the NLTHA. In the current implementation of the Lee damping model in OpenSees, the damping coefficient matrix C_d is assumed to be proportional to the structural tangent stiffness matrix [87]. The performance and issues of this approach have been discussed by Lee [88] and some details are briefly provided in Appendix III. The Lee damping model targets a constant elastic damping ratio ξ_{el} over an assigned frequency range, as shown in Figure 17, which complies with the basic assumption in the earthquake dynamics of structures better than Rayleigh damping [89]. The general drawbacks of Rayleigh damping has been discussed in detail [89,90]. Figure 17 shows ξ_{el} at the first natural frequency ($\omega_{f,s,1}$) and the second natural frequency ($\omega_{f,s,2}$) of a six-storey BRBGF structure with 2.5 mm initial slips as well as ξ_{el} at the first natural frequency ($\omega_{f,ws,1}$) of a six-storey BRBGF structure without initial slips. The BRBGF structure with initial slips had lower initial stiffness than that without initial slips and thus had a lower first natural frequency $\omega_{f,s,1}$ compared with $\omega_{f,ws,1}$. As shown in Figure 17, the Rayleigh damping model may slightly underestimate ξ_{el} when the slips of BRBGF structures are overcome and significantly overestimate ξ_{el} at higher modes compared with the Lee damping model. Therefore, the Lee damping model can avoid unrealistically high damping ratio predictions at higher modes. It also avoids spurious damping forces during the inelastic response [84].

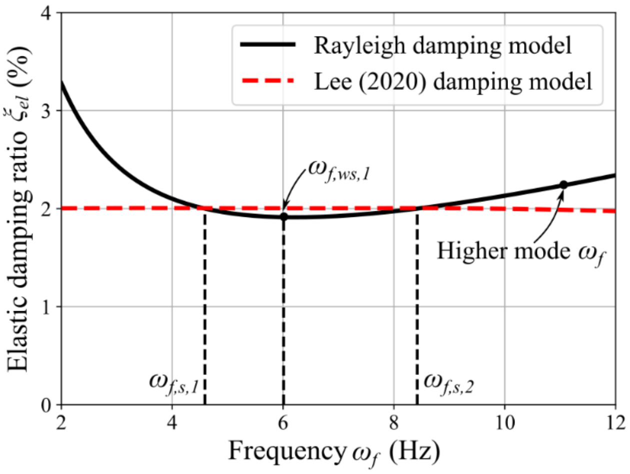

Figure 17 Comparison of damping ratio

4.4.2 Ground motion selection

The same ten ground motions listed in Table 3 were scaled to match the design acceleration and displacement spectra at the ULS with a return period of 500 years. The matching period is from 0.3–3.5 s, as shown in Figure 18, which is enough to cover the T_e of the buildings studied under this case. The scale factors are listed in Table 3 as SF2.

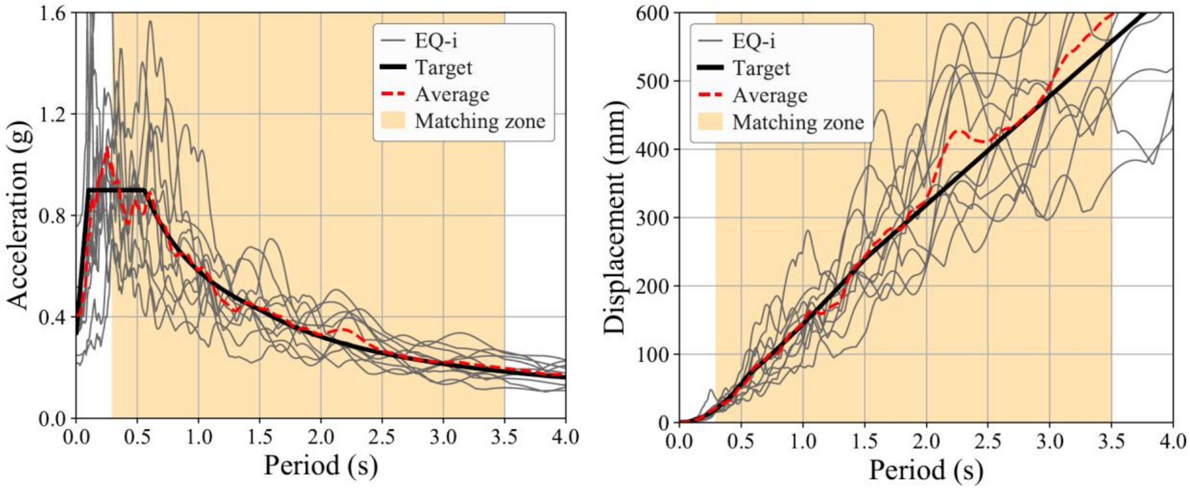

Figure 18 Acceleration spectrum and displacement spectrum matching

4.4.3 Displacement and inter-storey drift ratio response

Figure 19 shows the maximum displacement and inter-storey drift ratio (IDR) under each ground motion EQ-i from the NLTHA of the three BRBGFs compared to the mean and design target values. The mean values of the maximum IDR for BRBGF-6 and BRBGF-9 were 2.0% and 1.7% respectively, which are close to the design drift ratio θ_d (= 2.0%). The rest of IDR results were smaller than θ_d. The DDBD approach provided reasonably accurate and conservative predictions for the maximum displacement and IDR.

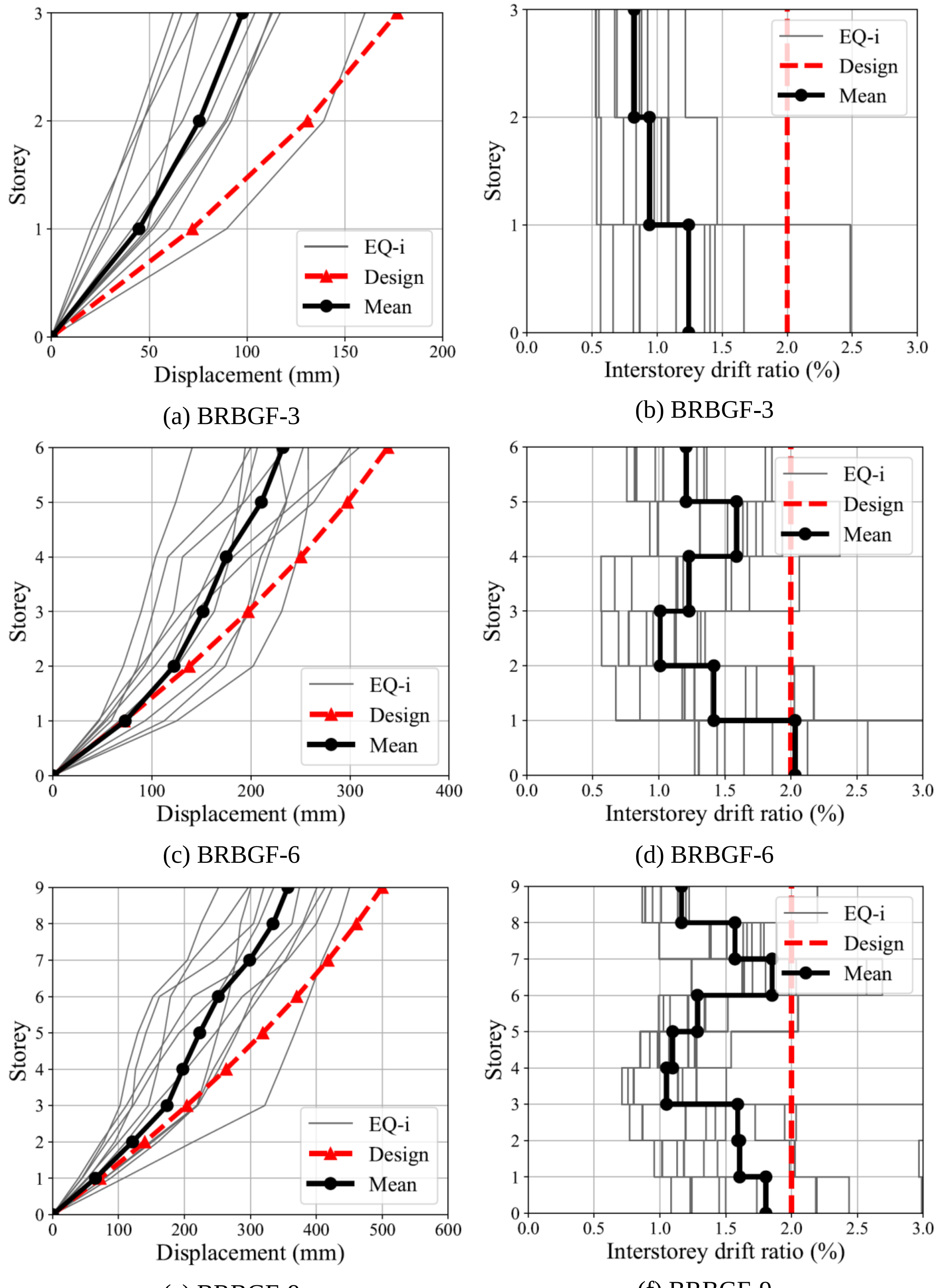

(a) BRBGF-3 (b) BRBGF-3

(c) BRBGF-6 (d) BRBGF-6

(e) BRBGF-9 (f) BRBGF-9

Figure 19 Maximum displacement profile and inter-storey drift ratio response

Figure 19 also shows that the IDR of the first storeys agreed better with the DDBD target drift than those of the upper storeys. One reason for this might be the actual shear force distribution along the height could be different from Eq. 16d because BRB frames are more sensitive to the formation of a soft storey [91]. The first storey was designed to have a higher ductility μ_1, as listed in Table 5, so it was expected to enter the yielding stage early. Once the first storey yielded, the stiffness of the storey decreased significantly. Thus, more deformations tended to concentrate on the first storey. Although the soft storey is a potential issue for BRB frames, the design examples illustrate that the DDBD approach can avoid excessive deformation concentration in one specific storey, and the displacement of BRBGFs is well controlled in general. It is also worth mentioning that the similarity between the actual displacement profile and the assumed profile is essential to ensure a good prediction of the DDBD approach [17]. Continuous columns at lower storeys are suggested for BRBGF systems to help avoid excess drift concentration on the first storey, so that the actual displacement profile of BRBGFs is close to the assumed displacement shape. Another reason for the slightly conservative predictions is that the cross-section design of BRBs (Eq. 25) neglects the strain hardening effect after yielding. As shown in Figure 19, the DDBD approach is more conservative for BRBGF-3 than for BRBGF-6 and BRBGF-9. The reason is that the average strain adjustment factor ρ_{avg} are 0.17, 0.35 and 0.32 for BRBGF-3, BRBGF-6 and BRBGF-9, respectively. The assumption of ρ_{avg} = 0.4 for BRBGF-3 overestimated the $\delta_{y,i,col}$ and underestimated the system ductility μ_{sys}. Because the BRBGF structures are more likely to work as LFRS for buildings with more than three storeys, it is suggested to use ρ_{avg} = 0.4 for the preliminary design. After the initial designs, further adjustments to ρ_{avg} along height can be made to optimise the configurations.

4.4.4 Glulam member strength check

The glulam members were all designed by considering the BRB overstrength factor γ_{BRB} = 1.5 to ensure they remained elastic under ULS loads. The maximum moments and axial forces in the columns and beams from the NLTHA were extracted. Eq. 27 from the New

Zealand Timber Structures Standard NZS 3603 [92] were used to check the beam and column strengths. Table 10 lists the glulam member sizes in the BRBGFs and the maximum combined strength factors (CSFs). The maximum CSF was 0.87 for columns and 0.69 for beams, so all glulam members satisfied the strength requirement.

$$CSF_1 = \frac{M_{t,mean}}{\phi_{GL} M_n} + \frac{N_{t,mean}}{\phi_{GL} N_{nt}} \leq 1.0 \qquad \text{Eq. 27a}$$

$$CSF_2 = \frac{M_{c,mean}}{\phi_{GL} M_n} + \frac{N_{c,mean}}{\phi_{GL} N_{nc}} \leq 1.0 \qquad \text{Eq. 27b}$$

where $N_{t,mean}$ and $N_{c,mean}$ are the mean values of the maximum tension and compression loads under ten ground motions (kN), respectively; $M_{t,mean}$ and $M_{c,mean}$ are the corresponding moments (kN·m) at $N_{t,mean}$ and $N_{c,mean}$, respectively; N_{nt} and N_{nc} are the nominal strength in tension and buckling (kN), respectively; M_n is the nominal bending strength (kN·m); and ϕ_{GL} (= 0.8) is the strength reduction factor for glulam.

Table 10 Combined strength factors of glulam members

	BRBGF-3				BRBGF-6				BRBGF-9			
Storey	Beam	*CSF**	*Col***	*CSF*	Beam	*CSF*	*Col*	*CSF*	Beam	*CSF*	*Col*	*CSF*
1	360×315	0.55	315***	0.52	405×315	0.69	360	0.87	450×315	0.64	540	0.61
2	360×270	0.43	315	0.33	405×315	0.52	360	0.61	450×315	0.58	540	0.56
3	360×270	0.30	315	0.03	405×270	0.44	360	0.34	405×315	0.53	540	0.40
4					405×270	0.42	270	0.56	405×315	0.45	405	0.58
5					315×270	0.49	270	0.44	405×270	0.46	405	0.48
6					315×270	0.27	270	0.03	405×270	0.45	405	0.29
7									405×270	0.42	270	0.57
8									315×225	0.52	270	0.49
9									315×225	0.30	270	0.03

Note: **CSF* is the maximum of CSF_1 and CSF_2 in Eq. 27; ***Col*= column; ***all columns are square.

It was also observed that the CSFs were primarily smaller than 0.7, and CSFs of the beams were generally smaller than those of the columns at the same storey. This is because the actual overstrength that the BRB reached during the NLTHA was smaller than γ_{BRB} (= 1.5). The actual axial deformation of BRBs was smaller than the ultimate deformation; therefore, the loads transferred to the glulam members were smaller than the design loads with γ_{BRB}. The beams had a large span (L = 8 m) and the moment load in the beam was proportional to L^2, which made the beams more sensitive to the design load level than columns. The member sizes can be optimised by using different γ_{BRB} along the height based on μ_i as suggested by Lopez and Sabelli [83], which beyond the scope of this study.

5 Conclusions

This study extended the DDBD approach to a new timber-steel hybrid multi-storey system that consists of glulam frames and BRBs. The design steps following the DDBD approach are discussed and critical design parameters are derived. The DDBD approach was then used to design three case studies of BRBGF structures with three, six, and nine storeys. NLTHA was conducted for the three buildings to verify the DDBD approach. The main conclusions drawn are as follows:

1) The inter-storey yield drift of BRBGFs must include the contribution of the BRB deformation, the column axial deformation and possible initial slips due to manufacturing tolerances for an accurate prediction of inter-storey yield drifts.
2) In contrast to BRB steel frames, the stiffness of connections between the BRBs and glulam frames in BRBGFs must to be considered. A stiffness adjustment factor λ (=0.72) was verified for the yield drift prediction of the BRBGF structures by pushover analyses.
3) The relationship between the spectral displacement reduction factor η and ductility factor μ for the Takeda fat model was also suitable for the BRBGF structures. It provided a slightly conservative prediction based on the results of NLTHA. The strength and stiffness of BRBs and initial slips caused by manufacturing tolerances had a negligible influence on the η-μ relationship.
4) The displacement profile for moment-resisting frames was also suitable for the BRBGF structures and provided relatively conservative predictions. The similarity between the

actual displacement profile and the assumed profile is essential to ensure a good prediction of the DDBD approach.

5) The maximum displacement and inter-storey drift response of the three BRBGF structures agreed reasonably well with the design target drift on the slightly conservative side. A soft-storey issue was not observed. Therefore, this study demonstrates that the DDBD approach can be a prospective methodology for the seismic design of BRBGF structures. Further investigations of the DDBD approach such as the optimisation design and risk-based evaluation are recommended for future study.

6 Acknowledgements

The authors acknowledge the Natural Hazards Research Platform, QuakeCore, University of Canterbury, and Shanghai Research Institute of Materials for sponsoring this project. The authors also appreciate the help of the lab technicians Russell McConchie, Alan Thirlwell, Michael Weavers, Peter Coursey and Dave Carney when preparing the manuscript.

7 Disclosure Statement

No potential conflict of interest was reported by the author(s).

8 Appendix

Appendix I Flowchart of the presented DDBD approach

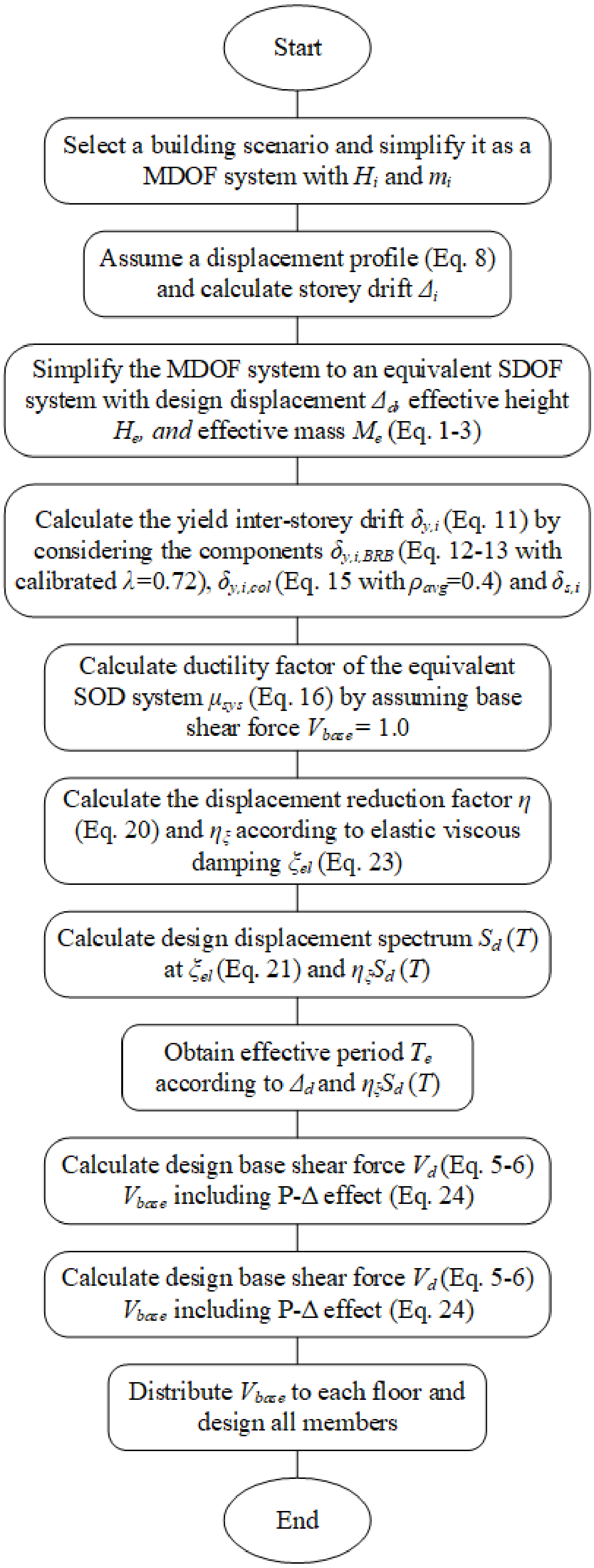

Appendix II Design procedure of BRBGF-6

The storey height information is listed in Table 5. The mass on each floor and roof (m_f and m_r) for BRBGF-6 can be calculated according to load information in Table 4 and NZS 1170.0 [93].

$$m_f = (D + 0.3Q) \times A_f/g = (1.8 + 0.3 \times 3.0) \times \frac{(40 \times 24)}{4 \times 9.8} = 65.6\ tons \qquad \text{Eq. A1}$$

$$m_r = (D + 0.0Q) \times A_f/g = (1.6 + 0.3 \times 3.0) \times \frac{(40 \times 24)}{4 \times 9.8} = 39.0\ tons \qquad \text{Eq. A2}$$

where D and Q are the dead load (kN) and live load (kN), respectively; A_f is the tributary area for each BRBGF (m^2).

The storey drift Δ_i is calculated based on the design drift ratio θ_d=2.0 and the displacement profile for MRF as shown in Eq. A3. Δ_i for each floor is listed in Table 5.

$$\Delta_i = \theta_d H_i \frac{(4H_6 - H_i)}{(4H_6 - H_1)} \qquad \text{Eq. A3}$$

The yield inter-storey drift contributions of the BRB deformation and the column axial deformation on the i-th storey are calculated by Eq. A4 and Eq. A5, respectively. The yield inter-storey drift for each storey along with the height of BRBGF-6 is calculated by Eq. A6 and the results are also listed in Table 5. The ductility factor for the i-th storey μ_i is thus calculated by Eq. A7. Eventually, the shear force on the i-th storey V_i in Eq. A8 can be calculated by assuming V_{base} = 1.0.

$$\delta_{y,i,BRB} = h_i \frac{2\varepsilon_y}{\lambda sin2\alpha} = h_i \frac{2\phi_m f_y}{\lambda sin2\alpha f_{sm} E_s} = \frac{3600 \times 2 \times 1.2 \times 235}{0.72 \times sin84^{\circ} \times 1.22 \times 210000} = 11.1mm \qquad \text{Eq. A4}$$

$$\delta_{y,i,col} = 2h_i \varepsilon_y \rho_{avg} \frac{\sum_{j=1}^{i-1} h_j}{L} = 2 \times 3600 \times 1.1 \times 10^{-3} \times 0.4 \times \frac{\sum_{j=1}^{i-1} h_j}{8000} \qquad \text{Eq. A5}$$

$$\delta_{y,i} = \delta_{y,i,BRB} + \delta_{y,i,col} + \delta_{s,i} \qquad \text{Eq. A6}$$

$$\mu_i = \frac{(\Delta_i - \Delta_{i-1})}{\delta_{y,i}} \qquad \text{Eq. A7}$$

$$V_i = \sum_{j=i}^{n} F_j \quad \text{Eq. A8a}$$

$$F_j = \begin{cases} 0.9\dfrac{m_j\Delta_j}{\sum_{i=1}^{n} m_i\Delta_i} V_{base} = 0.9\dfrac{m_j\Delta_j}{\sum_{i=1}^{n} m_i\Delta_i} & j < 6 \\ \left(0.1 + 0.9\dfrac{m_n\Delta_n}{\sum_{i=1}^{n} m_i\Delta_i}\right) V_{base} = 0.1 + 0.9\dfrac{m_n\Delta_n}{\sum_{i=1}^{n} m_i\Delta_i} & j = 6 \end{cases} \quad \text{Eq. A8b}$$

Appendix III Lee damping model

The Lee damping model has a damping matrix *C* and damping ratio *ζ* in a form of Eq. A9 and Eq. A10, respectively. The damping matrix *C* is symmetric, positive definite or semi-positive definite and possesses classical normal modes. The derivation can be found in [85].

$$C = \sum_{j=1}^{n_b} \left[M_{Cj} - M_{Cj}\left(M_{Cj} + K_{Cj}\right)^{-1} M_{Cj} \right] \quad \text{Eq. A9a}$$

where

$$M_{Cj} = 4\zeta_{pj}\omega_{pj}M \quad \text{Eq. A9b}$$

$$K_{Cj} = \frac{4\zeta_{pj}}{\omega_{pj}}K \quad \text{Eq. A9c}$$

and *M* and *K* are mass and stiffness matrix, respectively; ζ_{pj}, ω_{pj} are parameters that control the values and location of peak.

$$\zeta = \sum_{j=1}^{n_b} N(\omega, \omega_{pj})\zeta_{pj} \quad \text{Eq. A10a}$$

where $N(\omega, \omega_{pj})$ is a bell-shape based function as shown in Eq. A10 and Figure A1.

$$N(\omega, \omega_{pj}) = \frac{2\omega\omega_{pj}}{\omega_{pj}^2 + \omega^2} \quad \text{Eq. A10c}$$

and ω is the circular frequency.

Figure A1 shows the relationship between *ζ* and *ω* of the Lee damping model with five bell-shape based functions, which provides a almost constant damping ratio within desired frequency range [ω_{p1}, ω_{p5}]. The formulas for ζ_{pj}, ω_{pj} can be found in [84] and the configuration of Lee damping model.

This model has been implemented into local branch of OpenSees and suanPan [94] by the authors for the design verification, and will be been merged into main OpenSees repository in the near future.

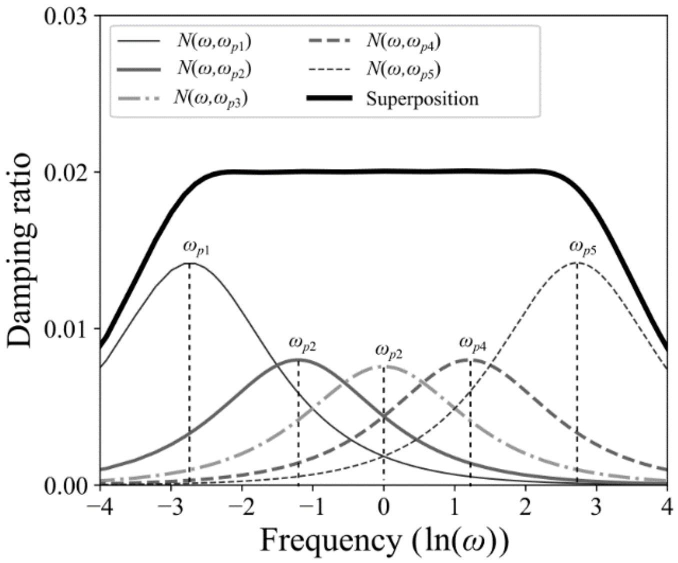

Figure A1. Damping ratio-frequency relationship of the Lee damping model

9 References

[1] Himes A, Busby G. Wood buildings as a climate solution. Developments in the Built Environment 2020;4:100030. https://doi.org/10.1016/j.dibe.2020.100030.

[2] Kirstein A, Siracusa J, Smith T. The new timber von Haast replacement building in Christchurch. 2018 NZSEE Conference 2018:1–9.

[3] Dickof C, Stiemer SF, Bezabeh MA, Tesfamariam S. CLT–Steel Hybrid System: Ductility and Overstrength Values Based on Static Pushover Analysis. Journal of Performance of Constructed Facilities 2014;28. https://doi.org/10.1061/(asce)cf.1943-5509.0000614.

[4] He M, Li Z, Lam F, Ma R, Ma Z. Experimental Investigation on Lateral Performance of Timber-Steel Hybrid Shear Wall Systems. Journal of Structural Engineering

2014;140:04014029. https://doi.org/10.1061/(asce)st.1943-541x.0000855.

[5] Dong H, He M, Christopoulos C, Li Z. Quasi-static tests and parametric simulations of hybrid steel frame and light wood shear walls with frictional dampers. Engineering Structures 2020:111485. https://doi.org/10.1016/j.engstruct.2020.111485.

[6] Brown JR, Li M, Palermo A, Pampanin S, Sarti F. Experimental Testing of a Low-Damage Post-Tensioned C-Shaped CLT Core-Wall. Journal of Structural Engineering 2021;147. https://doi.org/10.1061/(ASCE)ST.1943-541X.0002926.

[7] He M, Luo Q, Li Z, Dong H, Li M. Seismic performance evaluation of timber-steel hybrid structure through large-scale shaking table tests. Engineering Structures 2018;175:483–500. https://doi.org/10.1016/j.engstruct.2018.08.029.

[8] Quintana Gallo P, Carradine DM, Bazaez R. State of the art and practice of seismic-resistant hybrid timber structures. European Journal of Wood and Wood Products 2020. https://doi.org/10.1007/s00107-020-01556-3.

[9] Luo Q, He M, Chen F, Li Z. Probabilistic seismic performance assessment of timber-steel hybrid structures subjected to mainshock-aftershock sequences. Soil Dynamics and Earthquake Engineering 2021;141:106532. https://doi.org/10.1016/j.soildyn.2020.106532.

[10] Brown JR, Li M, Palermo A, Pampanin S, Sarti F, Nokes R. Experimental testing and analytical modelling of single and double post-tensioned CLT shear walls. Engineering Structures 2022;256:114065. https://doi.org/10.1016/j.engstruct.2022.114065.

[11] Gilbert CF, Erochko J. Development and testing of hybrid timber-steel braced frames. Engineering Structures 2019;198:109495. https://doi.org/10.1016/j.engstruct.2019.109495.

[12] Song X, Asce AM, Wu Y, Jiang H, Chen T. Lateral Performance of Glulam Timber

Frames with CFRP Confined Timber-Steel Buckling-Restrained Bracings 2022;148:1–16. https://doi.org/10.1061/(ASCE)ST.1943-541X.0003273.

[13] Granello G, Palermo A, Pampanin S, Pei S, Van De Lindt J. Pres-Lam Buildings: State-of-the-Art. Journal of Structural Engineering (United States) 2020;146:1–16. https://doi.org/10.1061/(ASCE)ST.1943-541X.0002603.

[14] Dong W, Li M, Lee C, Macrae G, Abu A. Experimental testing of full-scale glulam frames with buckling restrained braces. Engineering Structures 2020;222:111081. https://doi.org/10.1016/j.engstruct.2020.111081.

[15] Metelli G, Bregoli G, Genna F. Experimental study on the lateral thrust generated by core buckling in bolted-BRBs. Journal of Constructional Steel Research 2016;122:409–20. https://doi.org/10.1016/j.jcsr.2016.04.004.

[16] Dong W, Li M, Lee C, Macrae G. Numerical modelling of glulam frames with buckling restrained braces. Engineering Structures 2021;239:112338. https://doi.org/https://doi.org/10.1016/j.engstruct.2021.112338.

[17] Priestley MJN, Calvi GM, Kowalsky MJ. Displacement-based Seismic Design of Structures. IUSS Press; 2007.

[18] Kowalsky MJ, Priestley MJN, MacRae GA. Displacement Based Design of RC Bridge Structures. Proceedings of the Second International Workshop, 1994.

[19] Priestley MJN. Myths and Fallacies in Earthquake Engineering--Conflicts Between Design and Reality. Special Publication 1995;157:231–54.

[20] Priestley MJN. Myths and Fallacies in Earthquake Engineering , Revisited The Ninth Mallet Milne Lecture , 2003 2003:98.

[21] British Standard Institution (BSI). Eurocode 8: Design of structures for earthquake resistance 2005;1:1991–8.

[22] Australia and New Zealand Standards. NZS1170.5: Structural design actions - Part 5: Earthquake actions-New Zealand. Wellington, New Zealand: 2004.

[23] Maley TJ, Sullivan TJ, Corte G Della. Development of a displacement-based design method for steel dual systems with buckling-restrained braces and moment-resisting frames. Journal of Earthquake Engineering 2010;14:106–40. https://doi.org/10.1080/13632461003651687.

[24] Sullivan TJ. Direct displacement-based seismic design of steel eccentrically braced frame structures. Bulletin of Earthquake Engineering 2013;11:2197–231. https://doi.org/10.1007/s10518-013-9486-8.

[25] Erduran E, Yakut A. Drift based damage functions for reinforced concrete columns. Computers and Structures 2004;82:121–30. https://doi.org/10.1016/j.compstruc.2003.10.003.

[26] Medina RA, Krawinkler H. Evaluation of Drift Demands for the Seismic Performance Assessment of Frames. Journal of Structural Engineering 2005;131:1003–13. https://doi.org/10.1061/(asce)0733-9445(2005)131:7(1003).

[27] Ghobarah A, Abou-Elfath H, Biddah A. Response-based damage assessment of structures. Earthquake Engineering and Structural Dynamics 1999;28:79–104. https://doi.org/10.1002/(SICI)1096-9845(199901)28:1<79::AID-EQE805>3.0.CO;2-J.

[28] Salawdeh S, Goggins J. Direct displacement based seismic design for single storey steel concentrically braced frames. Earthquake and Structures 2016;10:1125–41. https://doi.org/10.12989/eas.2016.10.5.1125.

[29] Terán-Gilmore A, Ruiz-García J. Comparative seismic performance of steel frames retrofitted with buckling-restrained braces through the application of Force-Based and Displacement-Based approaches. Soil Dynamics and Earthquake Engineering

2011;31:478–90. https://doi.org/10.1016/j.soildyn.2010.11.003.

[30] Priestley MJN, Kowalsky MJ. Direct displacement-based seismic design of concrete buildings. Bulletin of the New Zealand Society for Earthquake Engineering 2000;33:421–44. https://doi.org/10.1201/9780849338090.ch4.

[31] Sullivan TJ, Priestley MJN, Calvi GM. Direct displacement-based design of frame-wall structures. Journal of Earthquake Engineering 2006;10:91–124.

[32] Pennucci D, Calvi GM, Sullivan TJ. Displacement-based design of precast walls with additional dampers. Journal of Earthquake Engineering 2009;13:40–65. https://doi.org/10.1080/13632460902813265.

[33] Belleri A. Displacement based design for precast concrete frames with not-emulative connections. Engineering Structures 2017;141:228–40. https://doi.org/10.1016/j.engstruct.2017.03.020.

[34] Yang B, Lu X. Displacement-Based Seismic Design Approach for Prestressed Precast Concrete Shear Walls and its Application. Journal of Earthquake Engineering 2018;22:1836–60. https://doi.org/10.1080/13632469.2017.1309607.

[35] Wijesundara KK. Seismic design of steel concentric braced frame structures using direct displacement based design approach. the 2nd international conference on sustainable built environments (ICSBE2012), Sri Lanka: 2012.

[36] Nievas CI, Sullivan TJ. Applicability of the direct displacement-based design method to steel moment resisting frames with setbacks. Bulletin of Earthquake Engineering 2015;13:3841–70. https://doi.org/10.1007/s10518-015-9787-1.

[37] Roldán R, Sullivan TJ, Della Corte G. Displacement-based design of steel moment resisting frames with partially-restrained beam-to-column joints. Bulletin of Earthquake Engineering 2016;14:1017–46. https://doi.org/10.1007/s10518-016-9879-6.

[38] Sahoo DR, Prakash A. Seismic behavior of concentrically braced frames designed using direct displacement-based method. International Journal of Steel Structures 2019;19:96–109. https://doi.org/10.1007/s13296-018-0092-0.

[39] Malla N, Wijeyewickrema AC. Direct displacement-based design of coupled walls with steel shear link coupling beams. Structures 2021;34:2746–64. https://doi.org/10.1016/j.istruc.2021.09.004.

[40] Filiatrault A, Folz B. Performance-Based Seismic Design of Wood Framed Buildings. Journal of Structural Engineering 2002;128:39–47. https://doi.org/10.1061/(asce)0733-9445(2002)128:1(39).

[41] Pang W, Rosowsky D V. Direct displacement procedure for performance-based seismic design of mid-rise wood-framed structures. Earthquake Spectra 2009;25:583–605. https://doi.org/10.1193/1.3158932.

[42] Zonta D, Loss C, Piazza M, Zanon P. Direct displacement-based design of glulam timber frame buildings. Journal of Earthquake Engineering 2011;15:491–510. https://doi.org/10.1080/13632469.2010.495184.

[43] Li Z, Wang X, He M, Dong H. Seismic Performance of Timber-Steel Hybrid Structures. II: Calibration of Performance Objectives and Design Method. Journal of Structural Engineering (United States) 2019;145. https://doi.org/10.1061/(ASCE)ST.1943-541X.0002424.

[44] Hashemi A, Zarnani P, Quenneville P. Seismic assessment of rocking timber walls with energy dissipation devices. Engineering Structures 2020;221. https://doi.org/10.1016/j.engstruct.2020.111053.

[45] Chen F, Li Z, He M, Wang Y, Shu Z, He G. Seismic performance of self-centering steel-timber hybrid shear wall structures. Journal of Building Engineering 2021;43:102530.

https://doi.org/10.1016/j.jobe.2021.102530.

[46] Thiers-moggia R, Málaga-Chuquitaype C. Performance-based seismic design and assessment of rocking timber buildings equipped with inerters. Engineering Structures 2021;248:113164. https://doi.org/10.1016/j.engstruct.2021.113164.

[47] Sullivan TJ, Priestley MJN, Calvi GM. A Model Code for the Displacement-Based Seismic Design of Structures DBD12. IUSS Press, PaviaTsakanika-Theohari E, Mouzakis H (2010) A post-byzantine mansion in Athens. The restoration project of the timber structural elements. In: Proceedings of the world conference on timber engineering. Trento, ItalyVamvatsikos D, Cornell C (2, vol. 31, 2012, p. 491514.

[48] Pettinga JD, Priestley MJN. Designed With Direct Displacement-Based Design. Journal of Earthquake Engineering 2005;9:309–30.

[49] Wijesundara KK, Rajeev P. Direct displacement-based seismic design of steel concentric braced frame structures. Australian Journal of Structural Engineering 2012;13:243–57.

[50] Gardiner S, Clifton GC, MacRae GA. Performance, damage assessment and repair of a multistorey eccentrically braced framed building following the Christchurch earthquake series. Steel Innovations Conference 2013, 2013.

[51] Dhakal RP, Pourali A, Tasligedik AS, Yeow T, Baird A, MacRae G, et al. Seismic performance of non-structural components and contents in buildings: an overview of NZ research. Earthquake Engineering and Engineering Vibration 2016;15:1–17. https://doi.org/10.1007/s11803-016-0301-9.

[52] McCormick J, Aburano H, Ikenaga M, Nakashima M. Permissible Residual Deformation Levels for Building Structures Considering both Safety and Human Elements. The 14th World Conference on Earthquake Engineering 2008:8.

[53] Park R. Evaluation of ductility of structures and structural assemblages from laboratory testing. Bulletin of the New Zealand Society for Earthquake Engineering 1989;22:155–66. https://doi.org/10.5459/bnzsee.22.3.155-166.

[54] Della Corte G. Vibration mode vs. collapse mechanism control for steel frames. Proceedings of the 5th International Conference on Behaviour of Steel Structures in Seismic Areas - Stessa 2006 2006:423–8.

[55] Vigh LG, Zsarnóczay Á, Balogh T. Eurocode conforming design of BRBF – Part I: Proposal for codification. Journal of Constructional Steel Research 2017;135:265–76. https://doi.org/10.1016/j.jcsr.2017.04.010.

[56] Zsarnóczay Á. Experimental and numerical investigation of buckling restrained braced frames for Eurocode conform design procedure development. Budapest University of Technology and Economics, 2013.

[57] Mahjoubi S, Maleki S. Seismic performance evaluation and design of steel structures equipped with dual-pipe dampers. Journal of Constructional Steel Research 2016;122:25–39.

[58] Jacobsen LS. Damping in composite structures. II WCEE, Tokyo, 1960 1960.

[59] Dwairi HM, Kowalsky MJ, Nau JM. Equivalent damping in support of direct displacement-based design. Journal of Earthquake Engineering 2007;11:512–30. https://doi.org/10.1080/13632460601033884.

[60] Grant DN, Blandon CA, Priestley MJN. Modelling inelastic response in direct displacement-based design 2005.

[61] Liu T, Zordan T, Zhang Q, Briseghella B. Equivalent viscous damping of bilinear hysteretic oscillators. Journal of Structural Engineering (United States) 2015;141:1–12. https://doi.org/10.1061/(ASCE)ST.1943-541X.0001262.

[62] Blandon CA, Priestley MJN. Equivalent viscous damping equations for direct displacement based design. Journal of Earthquake Engineering 2005;9:257–78. https://doi.org/10.1142/S1363246905002390.

[63] Wijesundara KK, Nascimbene R, Sullivan TJ. Equivalent viscous damping for steel concentrically braced frame structures. Bulletin of Earthquake Engineering 2011;9:1535–58. https://doi.org/10.1007/s10518-011-9272-4.

[64] Sullivan TJ, O'Reilly G. Characterising the Seismic Behaviour of Steel Beam-Column Joints for Seismic Design 2014.

[65] Khan E, Kowalsky MJ, Nau JM. Equivalent Viscous Damping Model for Short-Period Reinforced Concrete Bridges. Journal of Bridge Engineering 2016;21:1–12. https://doi.org/10.1061/(ASCE)BE.1943-5592.0000803.

[66] Loss C, Zonta D, Piazza M. Analytical model to evaluate the equivalent viscous damping of timber structures with dowel-type fastener connections. World Conference on Timber Engineering 2012, WCTE 2012 2012;2:516–25.

[67] Mazza F, Vulcano A. Equivalent viscous damping for displacement-based seismic design of hysteretic damped braces for retrofitting framed buildings. Bulletin of Earthquake Engineering 2014;12:2797–819. https://doi.org/10.1007/s10518-014-9601-5.

[68] Yahyai M, Rezayibana B. A simplified methodology to determine damping for special concentrically-braced frames. International Journal of Steel Structures 2015;15:541–55. https://doi.org/10.1007/s13296-015-9003-9.

[69] Yan L, Gong J, Zhang Q. Investigation of global equivalent damping and statistical relationship of displacement between nonlinear static and dynamic analysis of reinforced concrete frame structures. Earthquake Spectra 2018;34:1311–38.

https://doi.org/10.1193/021517EQS031M.

[70] Ghaffarzadeh H, Jafari A, Talebian N. Equivalent viscous damping in direct displacement-based design of steel braced reinforced concrete frames. The Structural Design of Tall and Special Buildings 2014;23:604–18.

[71] Landi L, Diotallevi P, Tardini A. Equivalent Viscous Damping for the Displacement-Based Seismic Assessment of Infilled RC Frames. 15th World Conference on Earthquake Engineering, 2007.

[72] Bezabeh MA, Tesfamariam S, Stiemer SF. Equivalent Viscous Damping for Steel Moment-Resisting Frames with Cross-Laminated Timber Infill Walls. Journal of Structural Engineering (United States) 2016;142. https://doi.org/10.1061/(ASCE)ST.1943-541X.0001316.

[73] British Standard Institution (BSI). Eurocode 8: Design of structures for earthquake resistance 1998.

[74] Pennucci D, Sullivan TJ, Calvi GM. Displacement reduction factors for the design of medium and long period structures. Journal of Earthquake Engineering 2011;15:1–29. https://doi.org/10.1080/13632469.2011.562073.

[75] Dong W. Seismic performance of glulam frames with buckling restrained braces (BRBs). University of Canterbury, 2021.

[76] British Standard Institution (BSI). 3: Design of Steel Structures: Part 1-1: General Rules and Rules for Buildings, BS EN 1993-1-1. BSI; 2005.

[77] American Institute of Steel Construction (AISC). Seismic provisions for structural steel buildings. ANSI/AISC 341-16. Chicago, IL: 2016.

[78] Aguaguiña M, Zhou Y, Zhou Y. Loading protocols for qualification testing of BRBs considering global performance requirements. Engineering Structures 2019;189:440–57.

https://doi.org/10.1016/j.engstruct.2019.03.094.

[79] Maley T, Sullivan TJ, Lago A, Roldan R, Calvi GM. Characterising the seismic behaviour of steel MRF structures. IUSS press; 2013.

[80] PEER. PEER NGA database. Pacific Earthquake Engineering Research (PEER) Center University of California, Berkeley, CA 2005. http://peer.berkeley.edu/nga/index.html.

[81] Houtte C Van, Bannister S, Holden C, Bourguignon S, Mcverry G. The New Zealand strong ground motion database. Bulletin of the New Zealand Society for Earthquake Engineering 2017;50:1–20.

[82] XLam NZ Limited. Designing With Xlam cross laminated timber. 2016.

[83] López W, Sabelli R. Seismic Design of Buckling-Restrained Braced Frames. 2004. https://doi.org/10.1139/l06-068.

[84] Lee CL. Proportional viscous damping model for matching damping ratios. Engineering Structures 2020;207:110178. https://doi.org/10.1016/j.engstruct.2020.110178.

[85] Lee CL. Sparse proportional viscous damping model for structures with large number of degrees of freedom. Journal of Sound and Vibration 2020;478. https://doi.org/10.1016/j.jsv.2020.115312.

[86] Lee CL. Bell-shaped proportional viscous damping models with adjustable frequency bandwidth. Computers and Structures 2021;244:106423. https://doi.org/10.1016/j.compstruc.2020.106423.

[87] Mazzoni S, McKenna F, Scott MH, Fenves GL. OpenSees command language manual. Pacific Earthquake Engineering Research (PEER) Center 2006.

[88] Lee C. Type 4 Bell-Shaped Proportional Damping Model and Energy Dissipation for Structures with Inelastic and Softening Response. Computers & Structures 2022;258:106663. https://doi.org/https://doi.org/10.1016/j.compstruc.2021.106663.

[89] Chopra AK, McKenna F. Modeling viscous damping in nonlinear response history analysis of buildings for earthquake excitation. Earthquake Engineering & Structural Dynamics 2016;45:193–211.

[90] Charney FA. Unintended consequences of modeling damping in structures. Journal of Structural Engineering 2008;134:581–92.

[91] Erochko J, Christopoulos C, Tremblay R, Choi H. Residual Drift Response of SMRFs and BRB Frames in Steel Buildings Designed according to ASCE 7-05. Journal of Structural Engineering 2011;137:589–99. https://doi.org/10.1061/(asce)st.1943-541x.0000296.

[92] New Zealand Standards. NZS3603:1993 Timber structures standard 1993.

[93] Australia and New Zealand Standards. ASNZS1170.0: Structural design actions - Part 0: General principles. structural design actions. vol. 2002. 2002.

[94] Chang T. suanPan- an open source, parallel and heterogeneous finite element analysis framework 2018. https://doi.org/https://doi.org/10.5281/zenodo.6108919.